FABRICATION AND CHARACTERIZATION
OF
SINGLE CRYSTALLINE SILICON SOLAR CELLS

A THESIS SUBMITTED TO
THE GRADUATE SCHOOL OF NATURAL AND APPLIED SCIENCES
OF
MIDDLE EAST TECHNICAL UNIVERSITY

BY

FIRAT ES

IN PARTIAL FULFILLMENT OF THE REQUIREMENTS
FOR
THE DEGREE OF MASTER OF SCIENCE
IN
PHYSICS

AUGUST 2010

Approval of the thesis:

FABRICATION AND CHARACTERIZATION OF SINGLE CRYSTALLINE SILICON SOLAR CELLS

submitted by **FIRAT ES** in partial fulfillment of the requirements for the degree of **Master of Science in Physics Department, Middle East Technical University** by,

Prof. Dr. Canan Özgen ______________
Dean, Graduate School of **Natural and Applied Sciences**

Prof. Dr. Sinan Bilikmen ______________
Head of Department, **Physics**

Prof. Dr. Raşit Turan ______________
Supervisor, **Department of Physics, METU**

Examining Committee Members:

Prof. Dr. Çiğdem Erçelebi ______________
Department of Physics, METU

Prof. Dr. Raşit Turan ______________
Department of Physics, METU

Prof. Dr. Macit Özenbaş ______________
Department of Metallurgical Engineering, METU

Prof. Dr. Tayfun Akın ______________
Department of Electrical and Electronics Engineering, METU

Assist. Prof. Dr. Emrah Ünalan ______________
Department of Metallurgical Engineering, METU

Date: *27.08.2010*

I hereby declare that all information in this document has been obtained and presented in accordance with academic rules and ethical conduct. I also declare that, as required by these rules and conduct, I have fully cited and referenced all material and results that are not original to this work.

Name, Last name : Fırat ES

Signature :

ABSTRACT

FABRICATION AND CHARACTERIZATION OF SINGLE CRYSTALLINE SILICON SOLAR CELLS

ES, Fırat

Master of Science, Department of Physics

Supervisor : Prof. Dr. Raşit TURAN

August 2010, 85 pages

The electricity generation using photovoltaic (PV) solar cells is the most viable and promising alternative to the fossil-fuel based technologies which are threatening world's climate. PV cells directly convert solar energy into electrical power through an absorption process that takes place in a solid state device which is commonly fabricated using semiconductors. These devices can be employed for many years with almost no degradation and maintenance. PV technologies have been diversified in different directions in recent years. Many technologies with different advantages have been developed. However, with more than %85 percent market share, Si wafer based solar cells have been the most widely used solar cell type. This is partly due to the fact that Si technology is well known from the microelectronic industry.

This thesis is concerned with the production of single crystalline silicon solar cells and optimization of process parameters through the characterization of each processing step. Process steps of solar cell fabrications, namely, the light trapping by texturing, cleaning, solid state diffusion, lithography, annealing, anti reflective coating, edge isolation have all been studied with a systematic approach. Each sample set has been characterized by measuring I-V characteristics, quantum efficiencies and reflectance characteristics. The best efficiency that we reached during this study is 10.37% under AM1.5G illumination. This is below the efficiency values of the commercially available solar cells. The most apparent reason for the low efficiency value is the series resistance caused by the thin metal contacts. It is observed that the efficiency upon the reduction of series resistance effect is reduced. We have shown that the texturing and anti-reflective coating have a critically important effect for light management for better efficiency values.

Finally we have investigated the fabrication of metal nanoparticles on the Si wafer for possible utilization of plasmonic oscillation in them for light trapping. The self assembly formation of gold nanoparticles on silicon surface has been successfully demonstrated. The optical properties of the nanoparticles have been studied; however, further and more detailed analysis is required.

ÖZ

TEK KRİSTAL SİLİSYUM GÜNEŞ GÖZELERİ ÜRETİMİ VE KARAKTERİZASYONU

ES, FIRAT

Yüksek Lisans, Fizik Bölümü

Tez Yöneticisi : Prof. Dr. Raşit TURAN

Ağustos 2010, 85 sayfa

Fotovoltaik güneş gözeleri kullanılarak elektrik enerjisi üretimi, dünyamızın iklimini tehdit eden fosil bazlı yakıtlara karşı en gelecek vadeden ve geçerli alternatiftir. Fotovoltaik piller, güneş enerjisini doğrudan elektrik enerjisine çeviren yarı iletken cihazlardır. Bu çevre dostu elektronik süreç, uzun yıllar bakım ve bozulmaya maruz kalmadan kullanılabilir. Fotovoltaik teknolojiler son yıllarda farklı alanlarda çeşitlilik kazanmıştır. Birçok avantjı olan farklı teknolojiler geliştirilmiştir. Buna rağmen, %85 pazar payı ile, Si pul tabanlı güneş gözeleri en yaygın kullanılan fotovoltaik sistemlerdir. Bunun bir nedeni, Si teknolojisinin mikro elektronik sanayide uzun yıllardır bilinen bir teknoloji olmasıdır.

Bu tez tek kristal güneş gözelerinin üretimi ve her bir üretim basamağının karakterizasyonu ile optimize edilmesi konularını kapsar. Yüzey şekillendirilmesi ile ışık hapsedilmesi, örnek temizliği, difüzyon, litografi, tavlama, yansıma engelleyici katman kaplama, kenar izolasyonu aşamaları, sistematik bir yaklaşımla incelenmiştir. Her örnek seti, akım voltaj ölçümleri, quantum verimliliği ve yansıma değerleri göz önünde bulundurularak karakterize edilmiştir. Bu çalışma süresince AM1.5G durumunda elde edilen en yüksek verim %10.37'dir. Bu değer, ticari olarak kullanılmakta olan göze değerlerinin altındadır. Bu düşük değerin en büyük nedeni ince metal kontaklardan kaynaklanan yüksek seri dirençtir. Seri direnç etkileri azaltıldığında verimliliğin arttığı gözlemlenmiştir.

Son olarak metal nanoparçacıkların Si pul üzerinde plazmonik salınımlarının ışık hapsedilmesi üzerindeki etkileri araştırılmıştır. Metal nano parçacıkların plazmonik saçılmaları, son yıllarda büyük ilgi çekmektedir. Altın nanoparçacıkların silisyum yüzeyi üzerinde kandiliğinden oluşumu başarıyla gözlemlenmiştir. Nano parçacıkların optik özellikleri incelenmiştir fakat göze verimi üzerindeki etkileri için daha fazla araştırma gerekmektedir.

ACKNOWLEDGMENTS

This thesis was carried out partly at Middle East Technical University (METU) Physics Department and partly at Micro Electro-Mechanical Systems (MEMS) Plant Clean Room for production. The thesis was financed by Ministry of Industry and Trade – Turkey as a part of the SANTEZ project ‘Production of Crystalline Silicon Solar Cells’.

I would like to thank Professor Raşit Turan for his support through all steps of this thesis and his guidance for my decisions along this period, Professor Tayfun Akın for giving me the opportunity work at MEMS facility, Mr. Harun Tanık for his broad mastership about semiconductor processing and Banu Kosif, Erdem Katı and Şerife Zor for their teamwork, METU MEMS clean room fab for providing the facilities for this work and staff for their help and friendship along this work. I would also like to thank Prof. Dr. Mehmet Parlak, Mustafa Kulakçı, Murat Kaleli, Mehmet Karaman, Zeynep Deniz Eygi, Urcan Güler, Ayşe Seyhan, Kutlu Kutluer, Yücel Eke, Sedat Canlı, Seçkin Öztürk, Döndü Şahin, Umut Bostancı Hakan Karaağaç, İrem Tanyeli and Burak Sefer, for their help about the facilities present in METU Physics Department and all Semiconductor Materials and Devices group and Solar Energy group for the beautiful friendship they showed for the last two years.

I also want to thank TUBİTAK for their financial support from the beginning of this graduate study.

Finally, I would like to thank my family for their patience along my studies and Selma Aydın for her great understanding and support during this work.

TABLE OF CONTENTS

CHAPTERS

LIST OF TABLES

TABLES

LIST OF FIGURES

FIGURES

ABBREVIATIONS

AM1.5G	Air Mass 1.5 Global
MWT	Metallization Wrap Through
EWT	Emitter Wrap Through
α-Si	Amorphous Silicon
CIGS	Cooper Indium Gallium Selenide
μc-Si	Micro Crystalline Silicon
BIPV	Building Integrated Photovoltaics
E_C	Conduction Band Energy
E_V	Valance Band Energy
eV	Electron Volt
KOH	Potassium Hydroxide
CZ	Czochralski
IPA	Iso Propyl Alcohol
DI	Deionized
Si	Silicon
e-	Electron
h+	Hole
E field	Electric field
SC	Semiconductor
PECVD	Plasma Enhanced Chemical Vapor Deposition
AR	Anti Reflective
TCO	Transparent Conductive Oxide

CHAPTER 1

INTRODUCTION

Solar energy is becoming more widely used for electrical power generation around the world with increasing need for renewable energies for environmental, economical and strategical reasons. Photovoltaics (PV) and the solar thermal generators are the two main technologies used for solar electricity production. Solar thermal generators reach efficiencies up to 29% with AC outputs easily adaptable to grid connection without any inversion [1]. However, maintenance at the movable parts, transmission losses, and requirements for high solar irradiation make solar thermal generators less appropriate for wide applications. On the other hand, in PV technologies, transmission losses may be eliminated by rooftop installations; electricity generation does not require high and direct solar radiation; and the almost no maintenance is required up to 25 years. These superior features make photovoltaics an attractive alternative for electricity generation.

In spite of its high potential of availability, solar energy has only been an academic interest for many years in Turkey. There has been almost no industrial activity in this field. While academic research groups have focused on some scientific problems of new technologies, the most standard and still the most feasible technology over the world, namely Crystalline Silicon Solar cell Technology has been missed out. One of the reasons for the lack of interest to crystalline solar cell technology is the belief that this technology has reached the maturity level which does not allow enough space for innovation. Although this is true at the first glance, recent developments in the crystal technologies have shown that new cell structures (like emitter wrapped through cells) can be developed for more efficient energy conversions. Second reason was that the process steps such as solid state diffusion need large infrastructure which is not widely available. The infrastructure available at METU has enabled us to carry out a complete solar cell production throughout this work and other projects. The clean room facilities of the MEMS Center of METU and the equipments such as diffusion furnaces and PECVD have been used for the device fabrication. Although MEMS facility is a micro electric center and it does not have specific instruments (like screen printers, lasers) for standard solar cell fabrication, it is still suitable for the demonstration of some basic technologies.

The aim of this M.Sc. study was to

1. Understand the basic structure and operating principles of Single Crystalline Silicon Solar Cells together with all production and characterization steps
2. Gain experience about production and characterization of single crystalline silicon solar cells.
3. Understand the effect of surface treatments on the solar cell performance.

Outline of the Thesis

The thesis is composed of 6 chapters, with the first one giving an introduction of the thesis, the objectives of the study and the outline of the thesis.

Chapter 2 starts with the general status of photovoltaics from beginning until today. Then a small introduction to different photovoltaic technologies is discussed. This is followed by basics of photovoltaic conversion with single crystalline silicon solar cell operation.

Chapter 3 includes all production steps used throughout the thesis study. The approach for each step is to explain the aim of the step followed by the theoretical considerations about the step and finally the experiment part where the experimental setup, procedure and the results are outlined.

Chapter 4 consists of the characterization of the solar cells. The parameters related to solar cell performance are given at the beginning of each part and experimental procedure and results are discussed at each part separately.

Chapter 5 consists of the self assembly formation of gold nanoparticles on silicon surface and the effect of surface plasmon resonance on reflectance spectrum for light trapping.

Chapter 6 includes a summary and conclusion of the thesis.

A bibliography for the research and appendices are given at the end of the thesis.

The thesis consists of 85 pages, 69 figures, 5 tables, 1 appendix and 20 references.

CHAPTER 2

PHOTOVOLTAICS GENERAL

2.1. Current Status of Photovoltaics

2.1.1. Historical Development of Photovoltaic Technology

The development of photovoltaic technology up to today's 42.8% efficient cells [2] starts with the Becquerel's discovery of photogalvanic effect in 1839 when he realized that the conductance of an electrolyte increased under illumination. Then in 1877 Adams and Day (UK) were to discover the photovoltaic effect on a junction between selenium and platinum which was the first observation of photovoltaic effect in solids. After several years of research and development in 1954, first 6% efficient Si solar cells were reported by Bell Labs, USA at the same time with 6% efficient Cu_2S/CdS solar cells by Air Force, USA [3].

In early years, most of the photovoltaic research was aimed for space applications with high cost and relatively high efficiency. As the technology began to mature in 1980's, low cost solar cells for everyday usage emerged with first MW plants installed in USA and Saudi Arabia [3]. The emerge of concentrated multijunction solar cells at 1980's enabled higher efficiencies from smaller areas of illumination and together with thin film solar cells they both decreased the raw material usage hence decreasing the initial costs. Then in 1990's low cost – low efficiency organic solar cells hit the market which offered ease of application and flexibility in large area integration. The development of photovoltaic performance along years can be seen at Figure 1.

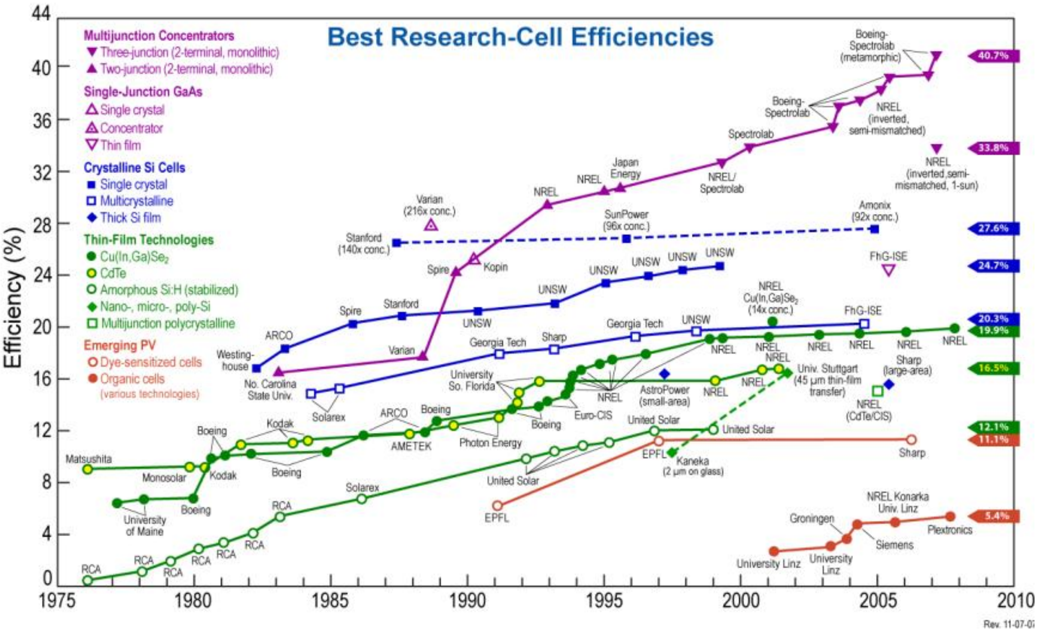

Figure 1: NREL's best research cell efficiencies graph [4]

2.1.2. Photovoltaic Market Today

Despite its fifty years of research and development, photovoltaic technology, like all other green technologies, was first considered to be alternative to the conventional fossil energy in the beginning of 1990's when EU recognized the CO_2 emissions are at dangerous rate for the earth's near future which will cause an estimated global warming of 1-4 C° by 2030. Until 1990's, photovoltaic applications on Earth were dominated with off-grid applications such as rural communication systems, meteorological systems, water pumping power supplies and small electronic devices. However by 1999 the installed PV generator capacity in PVPS (Photovoltaic Power Systems Program) countries was estimated to be a total of 500 MWp including off-grid and grid applications. Today, the total amount of installation reaches 23 GWp around the world (Figure 2).

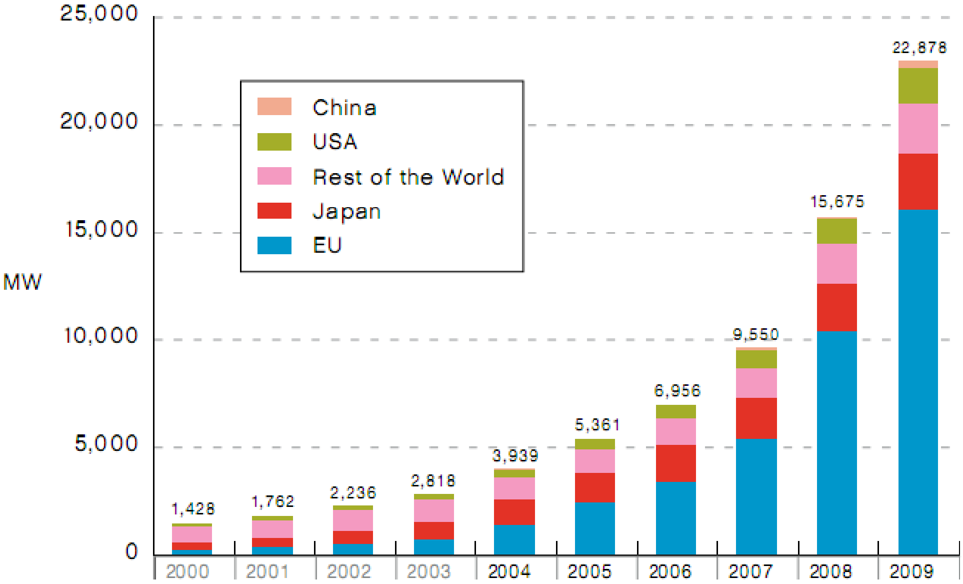

Figure 2: Total Installed PV capacity in the world [6]

The crystalline silicon technology still dominates the world PV market today [Figure 3]. According to PVPS, the wafer based module production was 2400 MW in 2007 while it is 300 MW for thin film based module production [5].

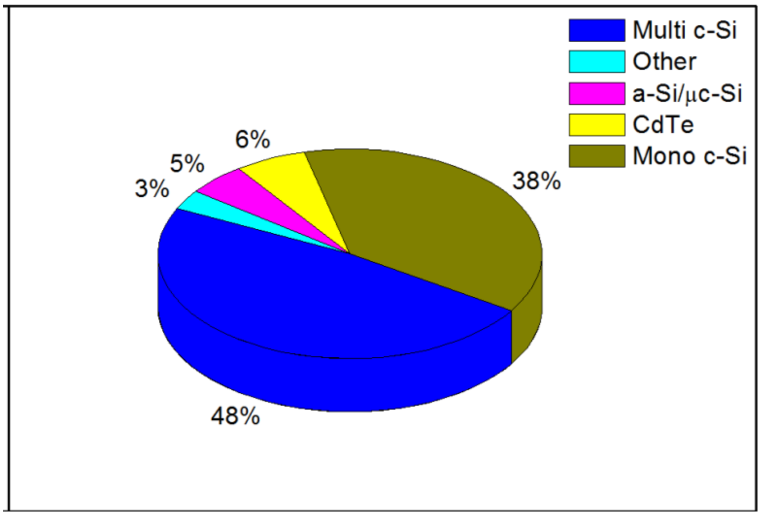

Figure 3 : Market shares of different photovoltaic technologies by the year 2008 [7]

The first reason why both multi and mono c-Si solar cells dominate the market is the abundance of Si which constitutes a big portion of the Earth's crust. Secondly, silicon is an element that has been used and studied for more than 30 years in semiconductor electronic industry so every step of silicon processing has matured more than any other elements'.

2.2. Photovoltaic Technologies

2.2.1. Single & Multicrystalline Silicon Solar Cells

Single and multicrystalline silicon solar cells are both wafer based technologies which are considered as the first generation solar cells (figure 4). While single crystalline silicon solar cells posses' higher efficiencies compared to multicrystalline silicon solar cells, the cost of producing single crystalline wafers is much higher than producing multicrystalline wafers. Consequently multicrystalline solar cell production holds the biggest share in the world market today compared to other technologies.

Figure 4: Industrial single crystal 156x156mm Solar cell [8]

Wafer based silicon solar cells have reached more than 24% cell efficiency and a 19.3% panel efficiency using different metallization and doping designs such as "Metallization Wrap Through", "Emitter Wrap Through" and back contact designs(Figure 5). All of those designs commonly solve the shading problems on the front surface, increasing the p-n junction area and easing the module production hence increasing the efficiency.

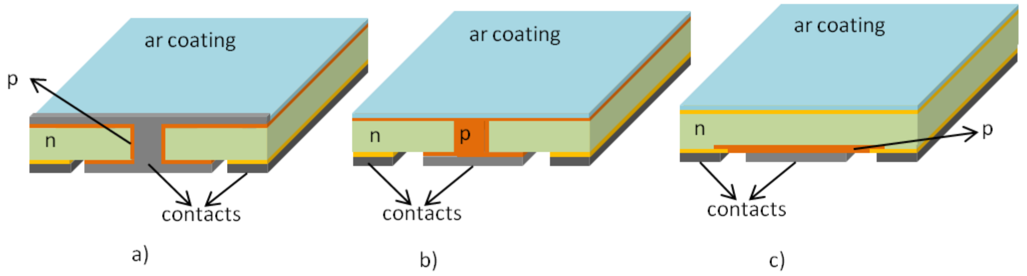

Figure 5: Metallization Wrap Through (a), Emitter Wrap Through (b), Back Contact designs (c)

2.2.2. Thin Film Solar Cells

The second generation photovoltaic cells are in the form of thin films which are deposited as a thin layer of photovoltaic material on thicker substrates. Some examples of solar cells in this group are α-Si (Figure 6) solar cells, Cd-Te solar cells, CIGS solar cells. The main advantage of thin film solar cells is their cost effectiveness due to low raw material usage. However, difficulty of deposition onto large areas is one of the problems that thin film industry faces today [9]. In addition, the efficiency of thin film solar cells is relatively low as compared to their wafer based counterparts which is a major drawback of thin film technology. Despite these difficulties, low cost and ability to be deposited on flexible substrates make thin film solar cells desirable when compared to wafer based silicon solar cells which must be joined together and laminated to form rigid solar panels.

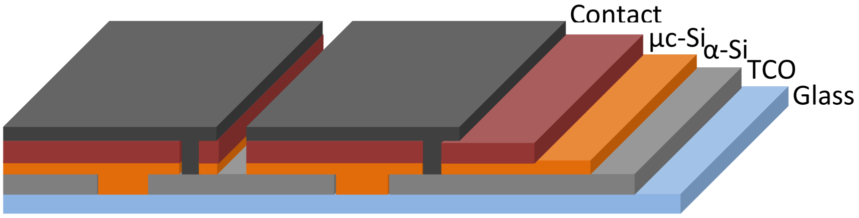

Figure 6: α-Si Solar Cell Structure

2.2.3. III-V semiconductors

III-V semiconductors such as GaAs, InAs, InP can be engineered to obtain different bandgaps from the same material family. III-V semiconductors with different bandgaps can be grown onto each other enabling different wavelengths of solar spectrum to be collected efficiently at each layer. However, due to high cost of the production of these materials, the solar devices of this kind are used under high concentration of sunlight to obtain higher power from smaller areas, reducing the cost of energy production. This type of solar cell system, which is commonly called Concentrated Photovoltaics (CPV), reaches record high efficiency values exceeding 40 %.

2.2.4. Organic Solar Cells

Organic solar cells can be produced using low cost polymers and can be deposited as very thin layers due to their high absorption coefficients. Therefore they are considered as the cheapest solar cells that can be produced. However, the efficiency and lifetime of these solar cells are very low compared to other solar cells. The highest efficiency reached with organic solar cells is about 6.5% obtained from a tandem structure [10]. The low efficiency and low lifetime of these cells can be compensated by application to large areas on flexible substrates, which is a very easy and low cost process based on roll to roll production technique.

2.2.5. Dye sensitized solar cells

Dye sensitized solar cells (DSSC) have emerged as an attractive low cost solar cell system recently. In this type of solar cells, dye molecules attached to TiO_2 nanoparticles are used to convert the solar radiation to electrical charge and collect them as an electrical current. Efficiency values up to 10 % have been reported for DSSC. Easy production process and relatively high efficiency values have made DSSC an attractive solar cell alternative to current technologies. DSSC can be fabricated with roll to roll production lines or by inject-printing. They can be used as transparent solar cells over windows enabling a more aesthetic and large surface integration in Building Integrated Photovoltaic (BIPV) applications.

2.3. Basic Principles of Photovoltaic Conversion

2.3.1. Solar Irradiation

Solar irradiation reaching earth's surface, which is 1,5x10^{11} meters away from the sun, is about 1350 W/m^2. The surface temperature of the Sun, which behaves like a blackbody source, is about 6000K. Consequently, the spectrum of sun at earth's surface is similar to any blackbody object whose surface temperature is at 6000K. However, as the radiation passes through the earth's atmosphere, some part of it is absorbed by different atoms and molecules present in the atmospheric layers; and some part is reflected and scattered. Finally the solar spectrum shown in the Figure 7 reaches the Earth's surface.

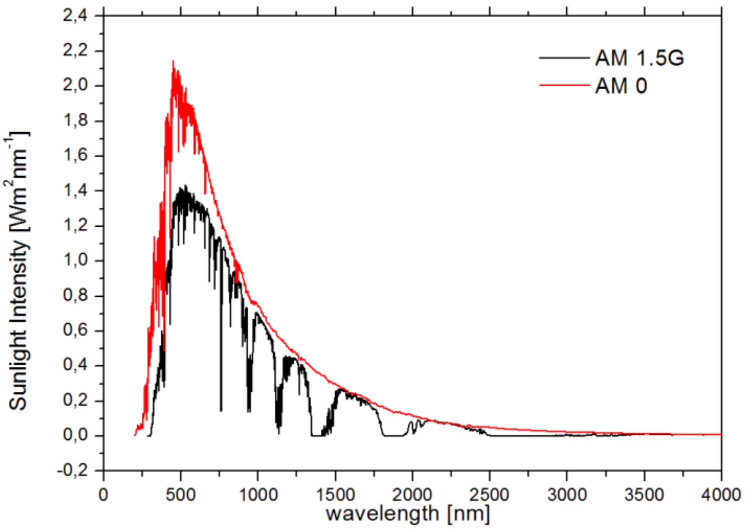

Figure 7: Solar irradiation at AM1.5G & AM0 [11].

The AM1.5 condition stated in the figure stands for '*air mass 1.5'*, which is a standard figure of merit for solar testing and characterization. Air mass is the amount of atmosphere thickness that the solar light travels and 1.5 is the condition on earth when the height of an object is equal to the length of its shadow. A general expression for the AM calculation is;

$$AM = \frac{1}{\cos \theta} \tag{1}$$

Where θ is the angle that the sun makes with the vertical and is 48° at AM1.5.

Other common standards are AM1 condition, which refers to the sun at the vertical direction and the AM0 condition, which refers to the radiation just outside the atmosphere. Also the difference in direct and diffuse radiation should be taken into the consideration. For AM1.5D, where D stands for *direct*, the radiation that is directly incident on the solar cell is taken into the account while for AM1.5G, where G stands for *global*, both direct and diffuse radiation from the atmosphere on the solar cell are considered.

2.3.2. Single crystal silicon solar cell structure

The structure of a basic single crystalline silicon solar cell is shown in Figure 8.

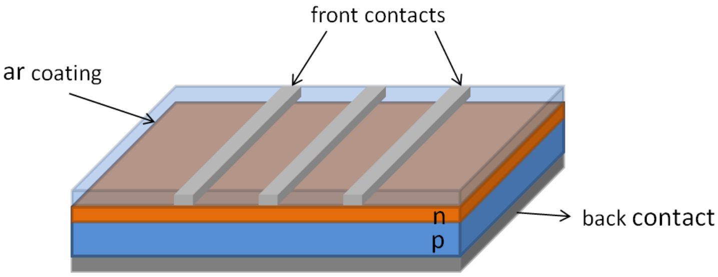

Figure 8: Structure of a single crystalline silicon solar cell

A p type single crystalline wafer is doped with group V elements (commonly phosphorous) to form a p-n junction close to the front surface. The front surface contacts are in grid form to enable light absorption in the p-n junction. The back side is fully metalized for better charge collection. Anti reflective coating enhances light absorption by decreasing the reflectance of the front side.

2.3.3. Single Crystalline Silicon Solar Cell operation

The process of power generation in a solar cell starts with absorption of light. When a photon with energy greater than or equal to the band gap of the semiconductor is incident on the cell, the energy of the photon is absorbed by an electron which in turn jumps to the conduction band, leaving a vacancy (hole) in the valance band of the crystal (Figure 9).

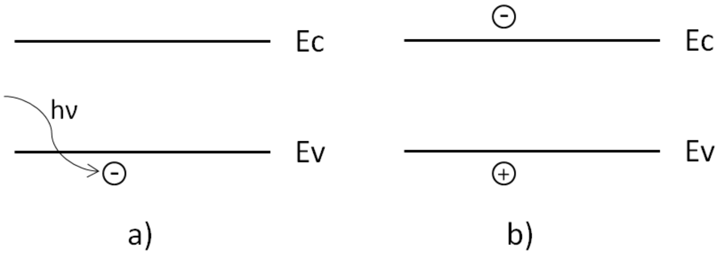

Figure 9: (a) a photon with energy hv ≥ Energy gap is absorbed by an electron (b) excited electron jumps to the conduction band leaving a hole behind in the valance band.

This process of creation of electron-hole pairs, which are charge carriers to be used in current generation, is called absorption. For solar cells the absorption affects the cell efficiency, since higher number of photons absorbed will create more electron hole pairs which will increase the current output of the cell. Therefore techniques such as surface texturing and anti-reflective coating are applied to improve the absorption in the active part of the solar cell.

Since the generated electron-hole pairs tend to recombine with time in the order of milliseconds, a mechanism to avoid this recombination is needed. A p-n junction formed across the cell is capable of separating these charge carriers before they recombine. The generated electron-hole pairs in the vicinity of the junction are separated by the built in electric field as shown in Figure 10.

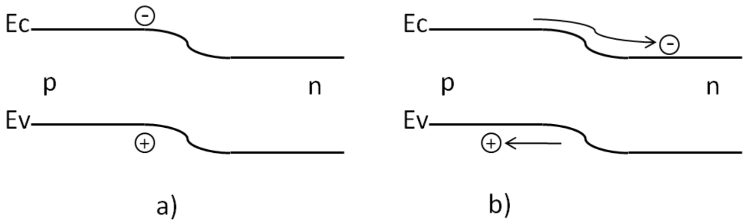

Figure 10: The generated electron hole pair (a) before separation, (b) after separation

After the separation, the electrons are collected by the contacts on the n side and holes are collected by the contacts at the p side to complete the photovoltaic power generation process.

2.3.4. Photovoltaic Cell Parameters

A solar cell consisting of a p-n junction exhibits typical diode behavior when dark I-V characteristic is concerned, which is described by the following equation.

$$I = I_0\left(e^{\frac{qV}{kT}} - 1\right) \tag{2}$$

where, *I* represent the current flowing through the cell, I_0 is the dark saturation current, V is the voltage applied between front and rear contacts, q is the electron charge, k is the Boltzmann constant and T is the absolute temperature in Kelvin. When the cell is illuminated, the cell starts to generate power and the I-V curve shifts in the vertical direction, taking the form

$$I = I_0\left(e^{\frac{qV}{kT}} - 1\right) - I_L \tag{3}$$

Where I_L is the light generated current.

Although the illuminated current shifts the I-V curve in the negative direction, conventionally the I-V curve of the solar cells is mirrored along the horizontal axis and shown as in Figure 11

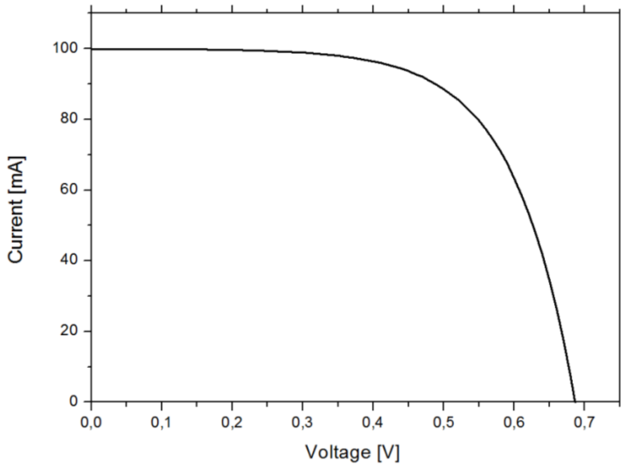

Figure 11: Illuminated I-V curve of a Solar Cell

Series resistance

The bulk resistance of the semiconductor used, the resistance due to metal-semiconductor interfaces and the resistance of the metal contacts all add to a total resistance which is called the series resistance. As the series resistance increases, the power loss due to resistive loses increase which has a negative effect on cell performance. The series resistance shows up on the illuminated I-V curve as the inverse slope of the I-V curve around open circuit voltage.

$$R_{series} = \frac{1}{\frac{dI}{dV}}\Bigg|_{V=V_{oc}} \tag{4}$$

Shunt resistance

Shunt resistance is a measure of the current leakage across the junction that may occur due to manufacturing defects. A high shunt resistance is needed to decrease leak currents for better cell performance. The shunt resistance is defined as the inverse slope of the illuminated I-V curve around short circuit current.

$$R_{series} = \frac{1}{\frac{dI}{dV}}\Bigg|_{V=0} \tag{5}$$

Open Circuit Voltage

When the cell is illuminated, there exists a voltage difference between the terminals of the solar cell if there is no current passing through the cell. This voltage difference is called the open circuit voltage (V_{oc}).

Short Circuit Current

Short circuit current (I_{sc}) is the current that flows through the cell when there is zero net voltage difference across the terminals of the solar cell. It depends on the number of carriers generated and collected through photovoltaic process. Therefore the cell area, reflectance and transmittance, light intensity and collection probability all affect the short circuit current of the solar cell.

Efficiency

Efficiency is defined as the ratio of the power output of the solar cell to the power input of the solar cell. At AM1.5 conditions, the power incident on a solar cell is about 1000Wm^{-2}. Therefore the efficiency can be defined as;

$$\eta = \frac{P_{out}}{1000\mathrm{W/m^2 xCell\ Area}} \tag{6}$$

The P_{out} is the max power output of the solar cell defined as maximum power point P_{max} (Figure 12).

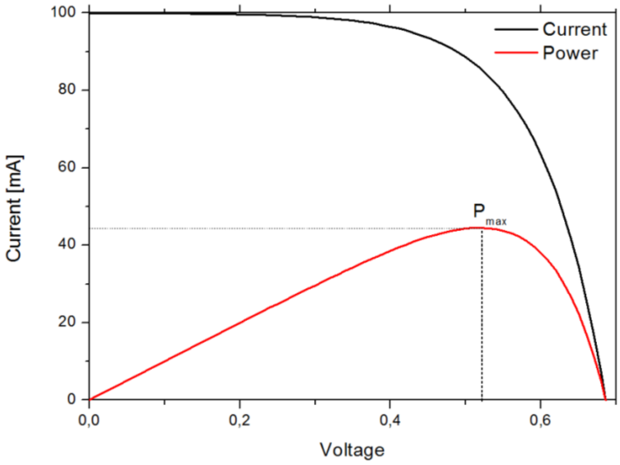

Figure 12: I-V and Power curve of a solar cell

Fill Factor

The voltage at P_{max} is defined as V_{max} and current at P_{max} is defined as I_{max}. For an ideal solar cell, the V_{max} will be equal to V_{oc} and I_{max} will be equal to I_{sc} therefore the I-V curve will have a perfect rectangular shape (Figure 13).

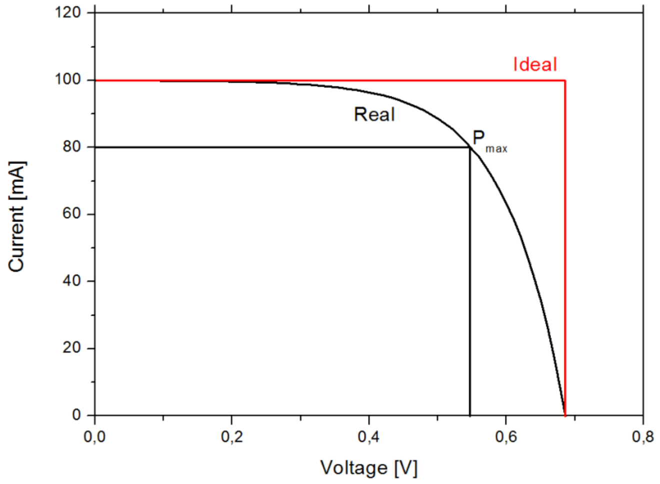

Figure 13: The ideal and real I-V curves

However, due to resistive losses the I-V curve deviates from a rectangle and fill factor is a measure of how close is the I-V curve of the cell to an ideal rectangular I-V curve. Therefore the fill factor is defined as;

$$ff = \frac{V_{max}\, I_{max}}{V_{oc}\, I_{sc}} \tag{7}$$

CHAPTER 3

PRODUCTION OF SINGLE CRYSTALLINE SILICON SOLAR CELLS

3.1. Introduction

The process steps followed for the preparation of the samples is given in the following chart.

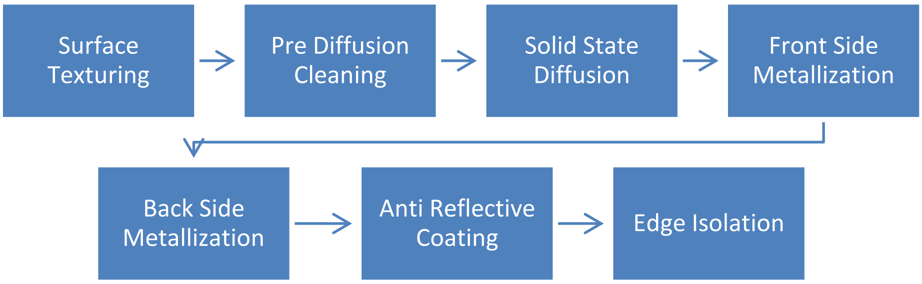

Chart 1: Process flow for sample preparation

The surface texturing step and the anti-reflective coating step were not applied to all sample sets to be able to make comparison on performance. The details of each step including the aim, theoretical considerations and the experimental part are discussed in the following sections of this chapter.

3.2. Surface Texturing

3.2.1. The Aim of Surface Texturing

Solar cells are devices that use photons to create electron hole pairs for photovoltaic conversion. Consequently, increasing the number of photons absorbed by the cell will increase the power output of the solar cell which is desirable for higher electricity generation. Silicon has a band gap of 1.12 eV implying that the useful spectral range for photovoltaic conversion is between 300-1100nm as shown in Figure 14.

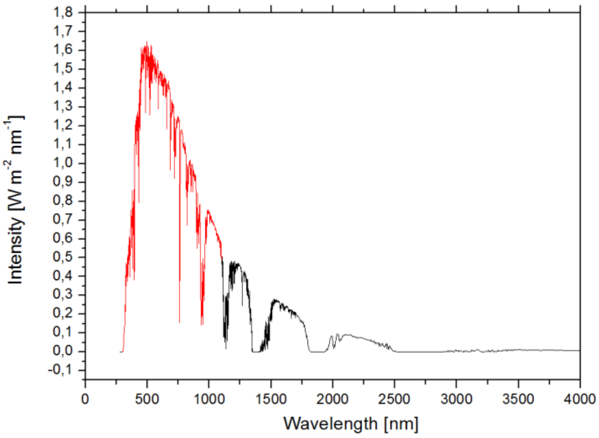

Figure 14: AM 1.5 spectrum at global tilt [12]

For a 90% absorption of the incoming intensity, the 300-1000nm portion of the spectral range is absorbed in a thickness of 400µm; however for a full absorption, the solar cell will have to be at a thickness of more than 2000µm [Figure 15].

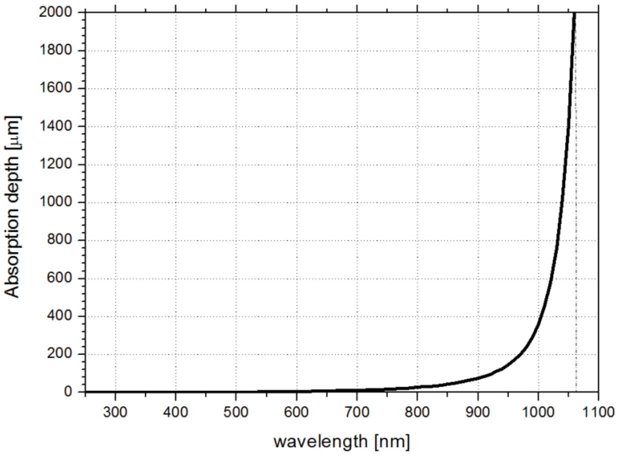

Figure 15: Absorption depth of Si for 90% absorption [13]

However, in a single crystalline Si solar cell, the generated electron-hole pairs are separated at the p-n junction who is close to surface and the pairs generated more than one diffusion length away from the junction has a very small chance to be collected by the external circuit. Therefore photons absorbed more than one diffusion length away from the junction will play no role on photovoltaic conversion. For silicon the minority carrier diffusion lengths are given as in Table 1.

Table 1: Minority carrier diffusion lengths in crystalline Si [14]

	n type	p type
Minority Carrier Diffusion Length	14 µm	140 µm

Consequently, there is a tradeoff between absorption and charge separation. For thicker cells, more photons will be absorbed but the created pairs will not be separated due to low diffusion lengths compared to the absorption depth. On the other hand, in thinner solar cells, all created pairs can be separated in the junction, however, in this case low energy photons will not be absorbed due to the poor absorption at long wavelengths.

Light trapping methods are commonly employed to overcome absorption problems in thin solar cells by increasing the total path traveled by the incident radiation in the cell through several internal reflections before being absorbed. Therefore, a mechanically thin solar cell will be seen thicker by incident rays. This will result in separation of electron hole pairs which are created by low energy photons, enabling a wider spectral range to be used in photovoltaic conversion and leading to an improved efficiency.

For single crystalline silicon solar cells, light trapping is accomplished by surface texturing which is usually done by an anisotropic etching process in KOH solution which creates a pyramidal structure on the surface. The pyramidal texture on the surfaces of the solar cell causes the incident rays to be refracted at an angle other than zero with the normal so that the rays will make several internal reflections inside the cell. This will increase the time that the photon spends inside the cell, and thus increase the probability of absorption to create electron-hole pairs as illustrated in Figure 16.

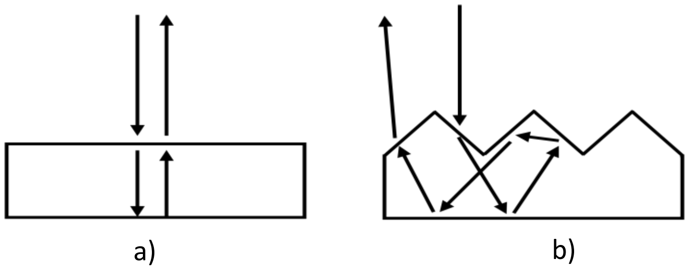

Figure 16: Light trapping of pyramidal structures on Single Crystal Si solar cells

Surface texturing of single crystalline silicon solar cells has another advantage on cell performance. The pyramid structures that form after texturing on the surface of the solar cell cause double reflection of light from the surface, therefore total reflectivity of the surface decreases from R to R^2 where R is reflectance with a value between 0 and 1 [Figure 17].

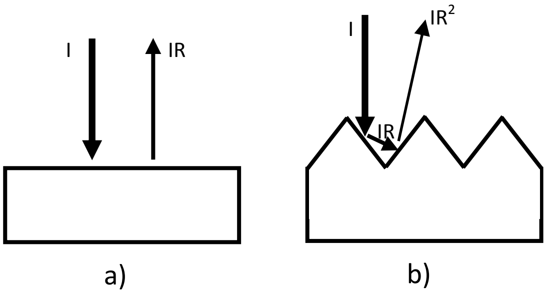

Figure 17: Reflection of a beam of intensity *I* from (a) un-textured surface, (b) textured surface. In (a), reflected beam has an intensity of *IR*, while in (b) reflected beam has an intensity of *IR²* due to double bouncing.

3.2.2. Theoretical Considerations of Anisotropic Etching

Anisotropic etching of silicon in aqueous KOH solution occurs according to the following mechanism [15];

$$Si + 4OH^- \rightarrow Si(OH)_4 + 4\,e^- \qquad (8)$$

The (100) and (110) planes have relatively high etch rates with respect to (111) planes (Table 2).

Table 2: Etch rates for different crystal planes at a given KOH concentration [15].

Etchant	**Etch Rate**		
	100	110	111
KOH %44, 85°C	1.4µm/min	2.8µm/min	4.6×10^{-3}µm/min
KOH %44, 85°C (relative)	300	600	1

Therefore, during the etching of a (100) oriented wafer, both (100) and (110) planes are etched very fast until all available surfaces have (111) planes only. This results in formation of small pyramids with walls having (111) orientations as shown in Figure 18.

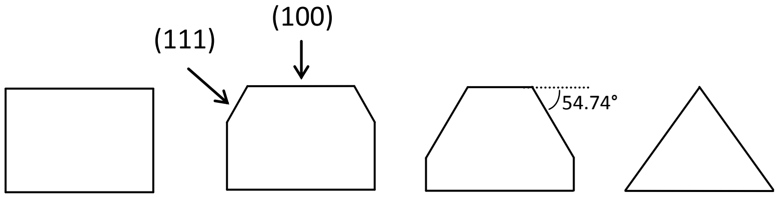

Figure 18: Anisotropic etching process of (100) oriented Silicon wafer. (100) and (110) plane are etched while (111) plane remains un-etched until pyramid structures start to occur with no (100) planes remaining.

3.2.3. Experiment

KOH texturing of silicon wafers was carried out in a 20 liters tank with a temperature controller, a N_2 bubbler and a magnetic stirrer. The N_2 bubbler and the magnetic stirrer were used to keep the solution homogeneous during the process. The temperature controller consists of a heater, a thermocouple and a controller.

The solution for the process is prepared with a total volume of 17.5 liters containing KOH, DI water and IPA. KOH used was in the form of 'ANYLSPEC', analytical reagent grade pellets. The solution was prepared inside the tank and the heater was set to the desired value. During the heating of the solution, the magnetic stirrer and N_2 bubbler was also set on to help KOH dissolve into the solution. Meanwhile, each sample was cut into four quarter pieces. The samples were CZ grown, boron doped, (100), top side polished silicon wafers, with Rs 0.1-1 Ω-cm, 1-5 Ω-cm, 5-10 Ω-cm, 10-20 Ω-cm.

For the first process, the wafers were dipped into 1:20 HF:DI solution before texturing to remove the natural oxide on the surface. After natural oxide removal, the wafers were dipped into the tank and the etching process started. During the etching process, the wafers were eye examined within each 3-4 minutes of intervals to be able to see the roughening of the surface (Figure 19). After the KOH etching, all wafers were cleaned and rinsed with DI water and dried with N_2. As can be seen from Figure 19, the reflection from the KOH etched sample is less than the unetched sample. The reflection properties will be examined in detail in the following sections.

Figure 19: The sample with and without surface texturing. It is seen that KOH etched surface (on the right side) has less reflection compared to the un-etched sample (on the left side)

3.2.4. Results

Surface texturing is an important process for light trapping in crystal Si solar cells. In this part of the study we carried out a series of experiments to understand and control texturing process with KOH based solutions. In order to have a complete process control we used different KOH, IPA (Isopropyl Alcohol) and deionized (DI) water concentrations.

The first observation was that the resistivity of the samples used did not have any drastic effect on texturing process. Figure 20 shows that wafers with different resistivity values have almost identical patterns after KOH etching process.

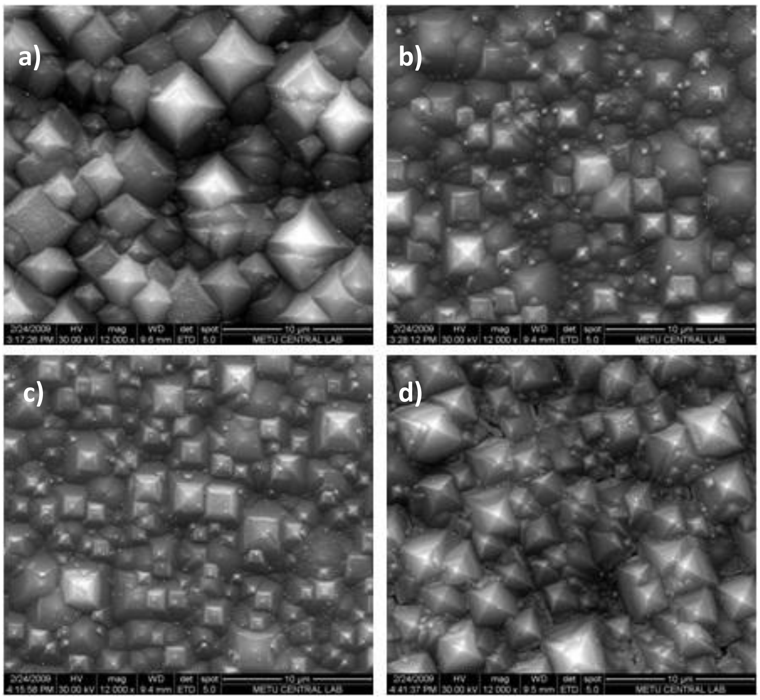

Figure 20: 2:88:10-KOH:DI:IPA concentration texturing of (a) 10-20Ω-cm,(b)5-10 Ω-cm, (c)1-5 Ω-cm, (d) 0.1-1Ω-cm wafers at 85°C for 10 min

Secondly we varied the KOH concentration to understand its effects on texturing process. It is generally observed that the decrease of KOH concentration increased the speed of formation of random pyramid structures as shown in figure 21. The shape of the pyramids was also affected by the variation of KOH concentration (Figure 21).

We observed that small variations in the solution temperature are not critical for the resultant patterns. As shown in figure 22, a temperature variation of 5 ^{o}C did not generate any difference in the shape and concentration of the surface pyramids.

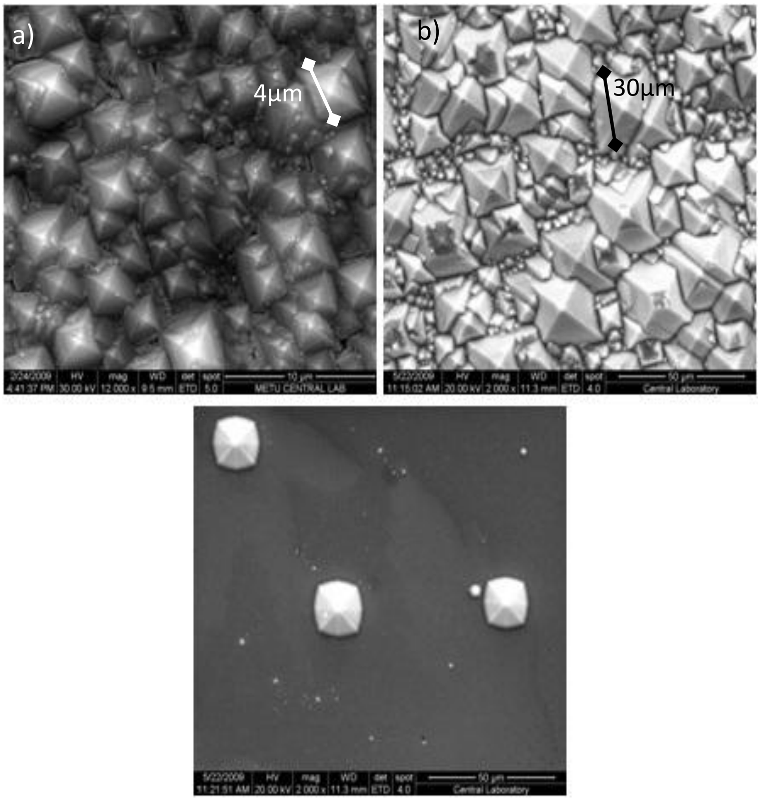

Figure 21: The effect of KOH concentration on pyramid formation. (a) 2% KOH 10 min, (b) 5% KOH 35 min, (c) 20% KOH 20 min. During the processes with 20% KOH, no surface roughening was observed.

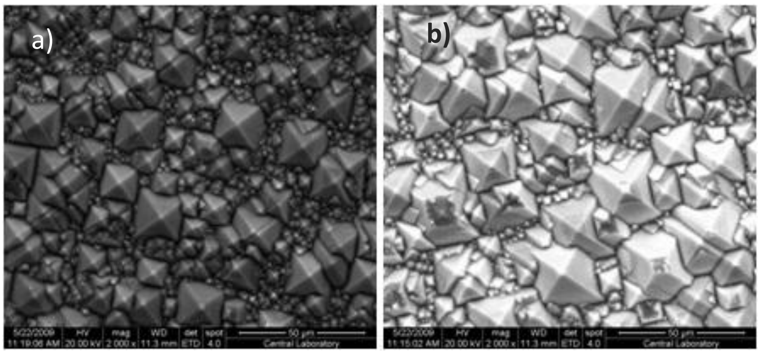

Figure 22: The effect of temperature on texture process, 5% KOH 35min at (a) 80°C, (b) 85°C

Throughout many experiments we carried out during this work, we observed that the IPA used in the solution did not have an active role on the etching process; however, addition of IPA, which has a lower density than DI water floated on top of the solution as a thick layer, prevented the evaporation of DI water and consequently helped the solution to remain at the same KOH concentration during the whole process. Therefore, although the process with 2% KOH solution at 85°C for 20minutes gave the pyramid structure as desired, the process with 5% KOH solution at 80°C for 35 and 45 min was to be chosen since the IPA started boiling at 85°C.

3.3. Pre Diffusion Cleaning

Before the solid state diffusion step, the wafers must pass through a cleaning cycle in order to get rid of all organic-inorganic contaminants and the natural oxide that may have grown on the wafer surface. For this purpose the so-called RCA cleaning steps were followed for all samples before the doping process. The cleaning procedure consisted of four main parts;

i. *Natural oxide removal:* In this step, the wafers were dipped into a 1:4 HF:DI Water solution at room temperature for about 30 seconds. The process stopped when the surface of the wafer became fully hydrophobic.

ii. *RCA 1:* After rinsing of the wafers with DI water, the wafers were dipped into a solution of H_2O_2: NH_4OH: DI with a concentration 1.5:1:6 at 70°C for seven minutes. In this step, organic contamination was removed from the wafer surface.

iii. *RCA 2:* After rinsing of the wafers, the last RCA step which removed heavy metal contaminants from the surface was applied. For this, the wafers were dipped into a 1.5:1:6 concentrations H_2O_2: HCL: DI solution at 70°C for 7 minutes and then rinsed at DI water again.

iv. *Natural oxide removal:* After the RCA 2 process, another oxide layer grows on the surface due to H_2O_2. This oxide was removed in a 1:4 HF: DI water solution at room temperature for 30 seconds as in the first oxide removal process.

At the end of the cleaning process, the wafers were rinsed in DI water and then dried in a centrifugal drier and became ready for solid state diffusion.

3.4. Solid State Diffusion

3.4.1. The Aim of Solid State Diffusion

The aim of solid state diffusion is the formation of the p-n junction across the wafer so that the created electron hole pairs can be separated for current generation. In an un-doped single crystalline Silicon lattice, which is called intrinsic Si, each Si atom shares four valance electrons with its neighboring Si atoms. When an impurity atom with three or five valance electrons substitutionally replaces a Si atom in the lattice, the electronic behavior of the crystal is changed. As illustrated in figure 23 b, if the substitutional impurity atom has five valance electrons, four valance electrons will be shared with neighbors and one excess electron will be free to move in the lattice. This type of material is called an n type material where the majority charge carriers are electrons. If the substitutional impurity atom has three valance electrons, there will be one electron missing in the covalent bonds of the Si atoms. This unoccupied state of electron is called a hole and this type of material where the charge carriers are holes are called p type materials (Figure 23 c).

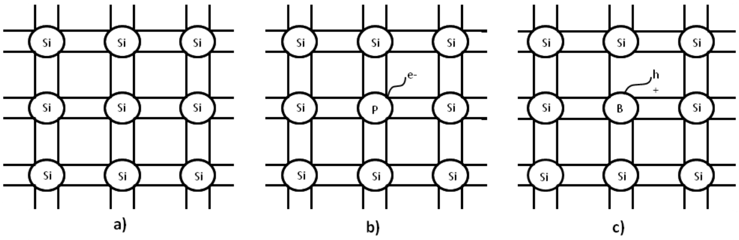

Figure 23: The crystal structure of (a) intrinsic Si, (b) Phosphorus doped n-type Si, (c) Boron doped p-type Si

When an n type and a p type material are brought together, there will be an electron flow from n type material to p type material and hole flow from p type material to n type material due to concentration gradient. However, since both regions were electrically neutral initially, the electrons passing to the p type material leave positive ions behind in the n region and holes passing to the n type material will leave negative ions in the p region. A region called depletion region is formed at the junction plane which is populated with an electric dipole. Therefore there will be a built in electric field inside the p-n boundary pointing from n region to p region (Figure 24).

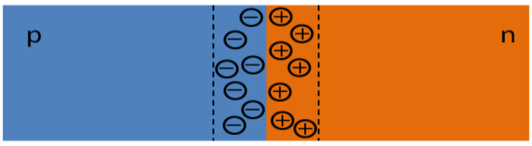

Figure 24: Cross Section of a p-n junction.

This electric field will counteract the diffusion of carriers due to concentration gradient and finally there will be an equilibrium where current due to concentration gradient is equal to current due to built in electric field. This built in electric field will cause the generated carriers be separated and used for power generation.

In practice, it is not possible to bring a p type material and an n type material together to create a p-n junction. One way to create a p-n junction is to dope the surface of an n type wafer with a group III (Boron) elements or alternatively to dope p type material with a group V (Phosphorous) element. During the doping process, the dopant atoms already residing in the crystal is compensated with the same number of opposite type dopant atoms introduced during the doping process. When the number of new dopants exceeds the native dopants in the surface region the type of the surface region is converted and two regions with different types of doping are created (Figure 25).

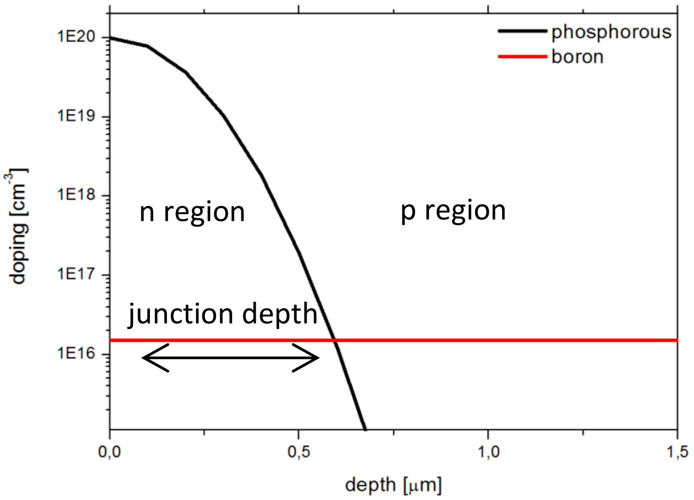

Figure 25: The concentration distribution for n-type doping a p-type material. At around 0.7 µm, the opposite type dopant concentrations are equal the junction is established there.

Crystalline Si is doped by a process called solid state diffusion in which, Si wafer is subject to the dopant atoms from the surface at high temperature and the dopant atoms diffuse into the material due to concentration gradient. With this process, the p-n junction described above can be formed across the surface of the wafer.

The depth of the junction and the doping concentration are the two key parameters that affect solar cells performance. If the p-n junction is deeper than one diffusion length from the front surface, the charge carriers created by high energy photons near the surface will not be able to survive and recombine before the separation. As for the dopant concentration, a higher doping will cause a better conductivity so the metal contacts will be better; however, high concentration means high number of defects which causes low diffusion lengths and has a negative effect on charge collection. So there is trade of between two cases and an optimum concentration level should be determined for the best device operation.

3.4.2. Solid State Diffusion Theory

Driving force in solid state diffusion is the difference of concentration of atoms. This process can be described by the transport equation called Fick’s First Law;

$$J = -D\frac{\partial\varphi}{\partial x} \tag{9}$$

Where J is the diffusion flux with dimensions of $mol/m^2.s$ representing the amount of matter incident to the surface per unit time per unit area, D is the diffusivity which is a property of the material and dopant atoms in dimensions of m^2/s and φ is the concentration of material in the units of mol/m^3. Additionally, the continuity states that the difference of flux through boundaries of an infinitesimal region is equal to change in concentration per unit time;

$$-\frac{dJ}{dx} = \frac{d\varphi}{dt} \tag{10}$$

By combining these two equations following diffusion equation is found;

$$\frac{d\varphi}{dt} = D\frac{d^2\varphi}{dx^2} \tag{11}$$

This equation may be solved for different boundary conditions. For an infinite source at the surface, as in the case of tube furnaces with constant dopant flow, the resulting concentration distribution will be in the form of a complementary error function;

$$C(x,t) = C_s \, erfc\left[\frac{x}{2\sqrt{Dt}}\right] \qquad (12)$$

Where C_s is the surface concentration of dopant atoms.

After predeposition, the concentration changes rapidly with dept and a more homogeneous distribution is desired. Therefore, a second diffusion step, *drive-in*, is usually applied to the predeposited wafers. In this step, the boundary conditions are such that there is a finite source of dopant atoms. The solution of diffusion equation for a finite dopant source is given as;

$$C(x,t) = \frac{Q}{\sqrt{\pi Dt}} exp\left(\frac{-x^2}{4Dt}\right) \qquad (13)$$

Where Q is the surface concentration introduced during predeposition. Consequently, the dopant distribution after all diffusion steps will be as shown in Figure 26.

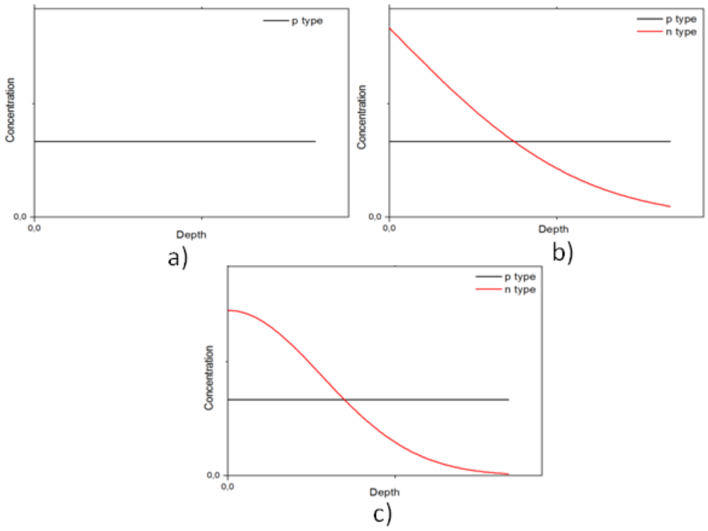

a) b) c)

Figure 26: Doping distributions along the wafer (a) before doping, (b) after predeposition, (c) after drive in

For n-type doping of Si liquid $POCl_3$ is commonly used. It is carried with N_2 to the furnace by a bubbler and O_2 is used to help $POCl_3$ deposition according to the chemical equations;

$$4POCl_3 + 3O_2 \rightarrow 2P_2O_5 + 6Cl_2 \qquad (14)$$

$$P_2O_5 + Si \rightarrow SiO_2(P) \qquad (15)$$

Phosphorus is embedded into the oxide layer and then diffuses into the wafer by concentration gradient. The $SiO_2(P)$ layer formed on the surface is called the Phosphosilicate glass and is etched from the surface after the doping process.

3.4.3. Experiment

Doping process was carried out in diffusion furnaces of METU-MEMS facility. The furnaces were tube type with three heating zones and were designed to process 4 inch wafers (Figure 27).

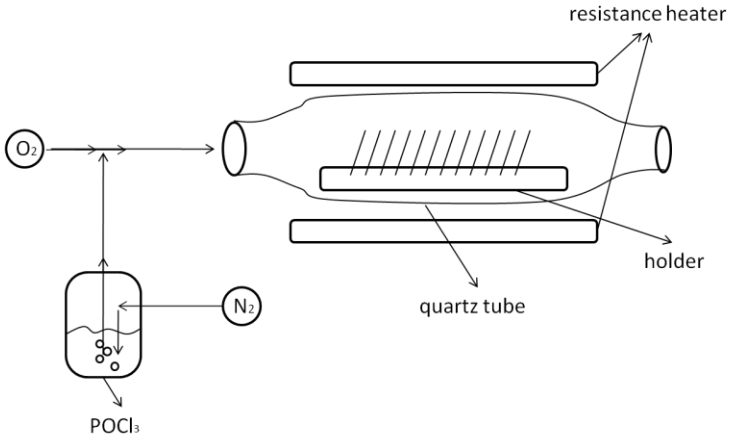

Figure 27: Tube furnace system for solid state diffusion

During the experiments, 4 inch, electronic grade, boron doped, single crystalline (100) round wafers with different doping levels were used. After the pre-diffusion cleaning, samples were placed in a quartz boat which was then inserted into the heated furnace in 3 minutes with a slow pace under N_2 flow. This avoided the thermal stress that may occur on the wafers due to abrupt temperature changes. Than the wafers were hold for 10 minutes inside the furnace to get them into a thermal equilibrium with furnace under O_2+N_2 environment. After temperature stabilization, the predeposition step was started with the flow of $POCl_3$+ O_2+N_2 followed by the drive process. After the drive-in step, all wafers were pulled out of the furnace again in 3 minutes and left for cooling for 15 minutes outside the furnace. For the last step, the phosphosilicate glass grown on the surface of the wafer was removed by etching in a 1:4 HF: DI water solution for 30 seconds. The wafers were then rinsed with water and dried with a drier.

After the doping, the sheet resistivity of the wafers was measured with the four point probe measurement tool. As shown in Figure 28, 5 different positions were selected for measurement on a wafer.

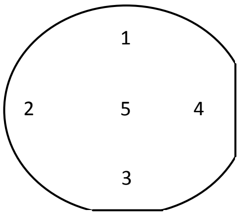

Figure 28: Wafers were tested by four point probe measurement tool from 5 different locations on the surface.

3.4.4. Results

The concentration profile of the doped P atom was determined by Secondary Ion Mass Spectroscopy (SIMS) with the newly installed SIMS facility at the METU Central Laboratory. The variation of the P concentration as a function of depth from the wafer surface is shown in figure 29. This result provides a direct evidence for the P doping in our experiments. It also shows that P profile is very much same as we expected from the theoretical consideration (see figure 25).

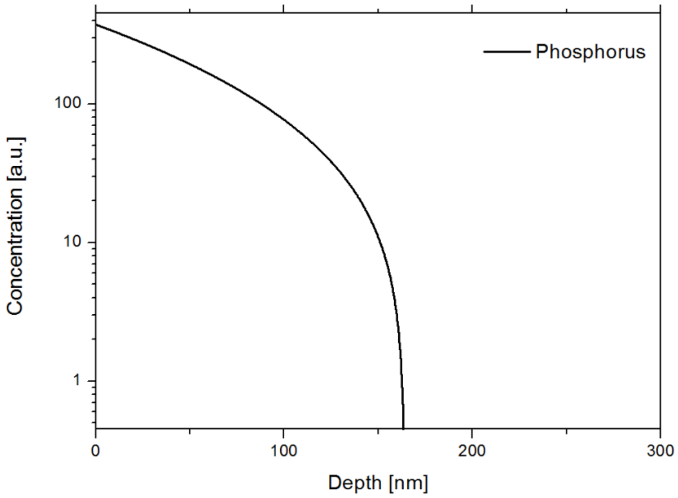

Figure 29: SIMMS result for sample 024 with 35Ω/□ sheet resistivity after 20 minutes of predeposition and 30 minutes of drive in at 850°C

The first observation about the doping experiments is that, the orientation of wafers relative to the gas flow inside the furnace has an effect on surface doping homogeneity. The wafers aligned perpendicular to the gas flow inside the furnace (Figure 30-a) showed higher standard deviations over the wafer surface while wafers aligned parallel to the gas flow (Figure30-b) showed smaller deviations on sheet resistivity (Figure 31).

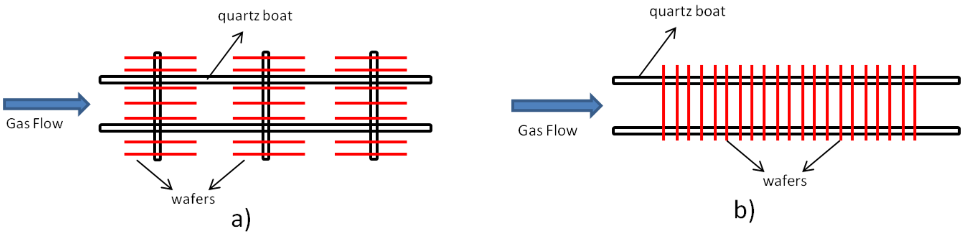

Figure 30: (a) wafers oriented perpendicular to the gas flow, (b) parallel to the flow

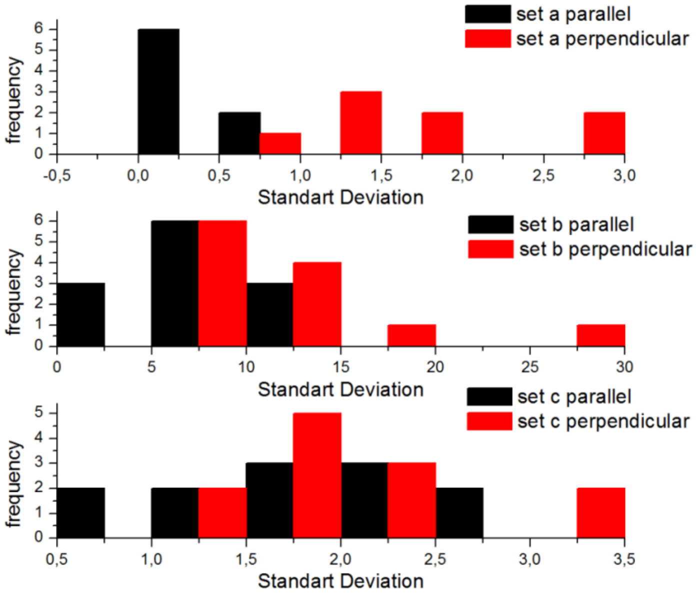

Figure 31: Standard deviations of sheet resistivity for three different sets. Set a is at 930 °C with 10 min predeposition and 30 min drive in. Set be is at 850 °C with 10 min predeposition and 30 min drive in. Set is at 850 °C with 20 min predeposition and 30 min drive in.

In order to understand the effect of deposition temperature on the resistivity, we run the system at two different temperatures by keeping all other process parameters constant. We observed that, the sheet resistivity decreased dramatically with increasing deposition temperature. However, the number of data point is not enough to reach reliable conclusions about the details of this effect. More experiments with systematic temperature variations are needed for this purpose.

In the final set of experiments we varied the predeposition duration for two different deposition temperatures. The variation in the sheet resistivity with predeposition duration is shown in Figure 32. We see that we obtained almost the same resistivity values for different predeposition time.

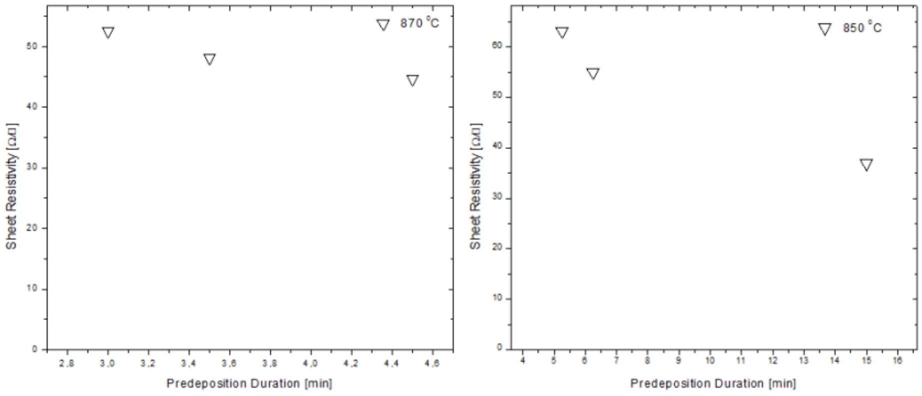

Figure 32: Effect of predeposition durations for samples with 25 minutes drive in.

The sheet resistivity is expected to be dependent on the drive in duration because the dopant distribution changes with time during the drive in process. Keeping all other process parameters constant, we determined the change in sheet resistivity with the derive in time as shown in Figure 33;

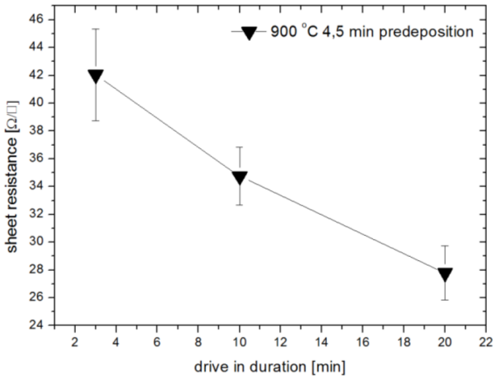

Figure 33: Variation of sheet resistivity with the drive-in duration for samples with 4.5 minutes of predeposition.

3.5. Metallization

3.5.1. Aim of Metallization

In order to carry the charge carriers separated by the p-n junction to an external load, metal terminals on p and n side is required. For this purpose, metallization is done at front and rear surfaces of the cells. Generally, the metallization on the front surface of the cell has a grid structure to let light into the solar cell while back side is fully covered. There are several ways of metallization used for solar cells such as, thermal evaporation, e-beam evaporation, screen printing etc.

3.5.2. Theory

Metallization aims to carry the separated charge carriers to an external load. Therefore the resistive losses due to contacts should be minimized to increase the efficiency of the solar cell. The main reasons of contact losses are the contact resistance and the resistance of the metal used.

Metals can form two types of contacts with semiconductor: Schottky contact which acts as a rectifying junction and ohmic contact where the I-V behavior is independent of the polarity of the applied voltage, (Figure 34).

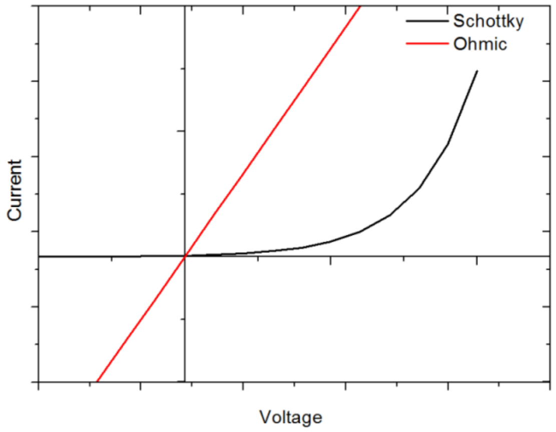

Figure 34: I-V behaviors of ohmic and Schottky contact

The type of the metal-semiconductor junction is generally determined by the work function difference between two materials. In the solar cell operation it is desirable to have minimum contact resistance at the metal-semiconductor junction. This can be accomplished either by an ohmic contact with low contact resistance or a Schottky junction whose forward bias direction is the same as the current flow during the solar cell operation.

When a metal and an n type semiconductor, with semiconductor work function lower than the metal work function is formed a Schottky barrier occurs. Also a p-type semiconductor with work function greater than the metal work function and the metal forms a Schottky junction. In each case, the opposite conditions lead to ohmic contact formation.

Schottky junction formation can be avoided by heavily doping the semiconductor side of the metal semiconductor junction. In this way the current through the junction is carried by the tunneling effect which provides very low contact resistance.

The resistance also depends on the geometry of the metal contacts on the solar cell. The fingers and the busbars carry the current and must have low resistances. Therefore, thick layers of metals will have better conductivity on the surface

$$Aspect\,ratio = \frac{Height}{Width} \tag{16}$$

is an important parameter. In order to have the optimum conductivity values with maximum illumination, we should be able to increase the thickness of the metal. This condition is illustrated in figure 35. This is however not easy with vacuum evaporation and lithography. The screen printing method is more appropriate for such improvements during the metallization.

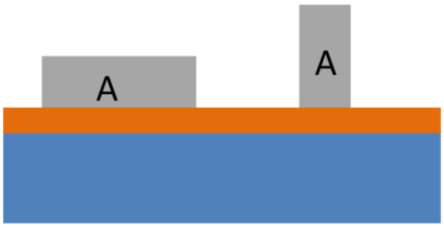

Figure 35: The resistance is given by $R = \frac{\rho l}{A}$, therefore the larger the area, the better will be the conductivity. However the aspect ratio of the metal geometry is also important. Two patterns with same cross section area are shown in the figure. For solar cell applications the one with small width and bigger height is preferred to have maximum illumination with the same conductivity.

3.5.3. Metallization by e-beam evaporation and lithography

Although the screen printing technique is generally preferred for large applications vacuum evaporation and lithography are used for research purposes. As mentioned above, in the vacuum evaporation techniques, the film thickness is limited to a few micrometers which is not thick enough for solar cell applications. In this work we have used e-beam evaporation systems available at Physics Department and MEMS facility. In order to form metal grid pattern on front surface of the solar cell, first, front side of the cells were entirely coated with Al. The e-beam evaporator was operated at 10^{-5} mbar pressure and with an evaporation rate of 15Å/s. The process was stopped when the film thickness has reached about 1-2µm which was monitored by a quartz thickness oscillator. After the coating is completed, the thickness of the Al was confirmed by an M-Gauge thickness measurement tool. The wafers were then annealed at 450°C for 30 min under N_2 flow. Then the coated top sides of the wafers were spin coated with photoresist S 1813 at 500rpm for 7s and 2000rpm for 30 s and were baked at 115°C for 70 s. The wafers were then loaded into the lithography system where they were exposed to the UV light for 10 seconds through a glass mask with the desired metallization pattern. Two different front side masks (figure 36) with the pattern parameters shown in the table shown below were used.

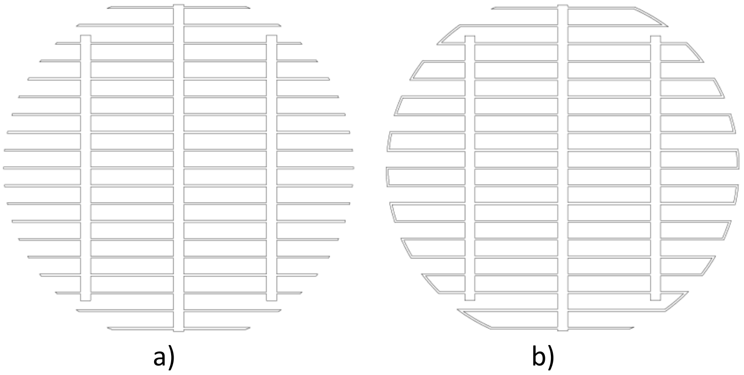

Figure 36: Designs of (a) mask 1, (b) mask 2

Table 3: Parameters of the two mask designs

	Mask 1	Mask 2
Finger Width [µm]	220	350
Busbar Width [µm]	2000	2000

After the UV exposure, the photoresist was developed with a solution called MF-319 for 1 min and rinsed and dried. Since a positive photoresist was used in this work, the photoresist area exposed to the UV light was removed, leaving behind the same pattern of the glass mask. The Al was etched away in H_3PO_4 %78.5 CH_3COOH %15, HNO_3 %1,5 , H_2O %5 solution until Si can be recognized clearly at 42°C and then wafers were rinsed and dried again. Last operation was the removal of the last photoresist layer over the metal contacts with PRS 2000 at 82°C for 15 minutes and the wafers were then rinsed and washed again to get ready for back contact metallization.

3.5.4. Results

Back contact metallization was done in the same way as the front side, however, for some samples, metal ring masks were used as shadow masks during the evaporation to avoid shunts with front surfaces. The pictures of different solar metallization pattern obtained in this work are shown in figure 37.

Figure 37: Two different front grid patterns, left one prepared with mask 1, right one prepared with mask 2

The aspect ratio reached in evaporation is 0,007 for fingers and 0,001 for busbars of the mask 2, and 0,011 for fingers and 0,001 for busbars of the mask 1. These values are far from the desired aspect ratio in a typical solar cell structure. The effect of poor aspect ratio is seen in the solar cell results that will be presented in the following chapters.

3.6. Anti Reflective Coating

3.6.1. The aim of anti-reflective coating

The number of photons absorbed is a key factor that determines the current output of a solar cell. An increase in the number of photons absorbed increases the current output and vice versa. It is then desirable to reduce the reflection from the cell surface and direct the incoming photons into the device active region. Silicon having a reflection spectrum given as in Figure 39 has an average of 35% reflectance at visible region.

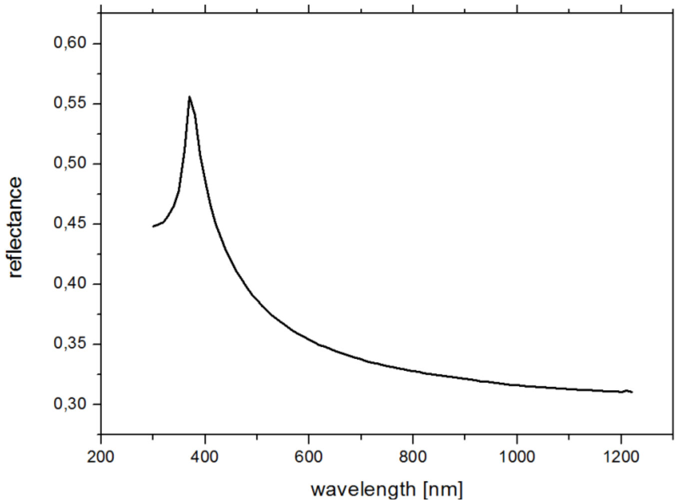

Figure 38: Reflectance Spectrum of Bare Silicon [16]

To increase the number of photons absorbed by the solar cell, anti-reflective (AR) coating thin films are usually applied to the surfaces of the solar cells. These coatings decrease the reflected intensity nearly to zero around at some specific wavelengths and have a great effect on solar cell performance.

3.6.2. Theory

For solar cells, anti reflective coatings act as interference filters that avoid the reflection of light back from the surface. Thin films grown on the surface cause destructive interference between reflected rays from the substrate and the film, hence the net reflected intensity becomes zero [14].

The reflectance from a medium with refractive index n_0 to another with index n_s is given by;

$$R = \left(\frac{n_0 - n_s}{n_0 + n_s}\right)^2 \tag{17}$$

For substrates coated with dielectric thin films, the reflection spectrum changes as [14];

$$R = \frac{(n_0 - n_s)^2 + \left(\frac{n_0 n_s}{n_a} - n_a\right)^2 \left(\tan\frac{2\pi n_a t\cos\theta}{\lambda}\right)^2}{(n_0 + n_s)^2 + \left(\frac{n_0 n_s}{n_a} + n_a\right)^2 \left(\tan\frac{2\pi n_a t\cos\theta}{\lambda}\right)^2} \tag{18}$$

Where n_0 is the refractive index of the medium from which light is incident, n_a is the film refractive index, n_s is the substrate refractive index, λ is the wavelength at which reflectance is calculated and θ is the angle of incidence. For normal incidence (θ = 0) the reflectance makes minimum at;

$$n_a = \sqrt{n_0 n_s} \tag{19}$$

and at;

$$t = \frac{\lambda}{4n_a} \tag{20}$$

The refractive index of the anti-reflective film and the thickness of that film can be calculated using these equations. For silicon with $n_s = 3{,}44$ [17] with light incident from air with $n_0 = 1$, the optimum anti-reflective coating refractive index is calculated as;

$$n_a = \sqrt{3{,}44} = 1{,}87 \qquad (21)$$

The thickness of the film with index 1.87 with reflectance minimum at 600nm is found as;

$$t = \frac{600}{4 \times 1{,}87} = 80.2\ nm \qquad (22)$$

600 nm is chosen because the solar spectrum has the maximum value at this wavelength.

The reflectance spectrum for an anti-reflective coating of refractive index 1.87 and thickness 80nm were then calculated using the above equation as a function of the wavelength and displayed in Figure 39.

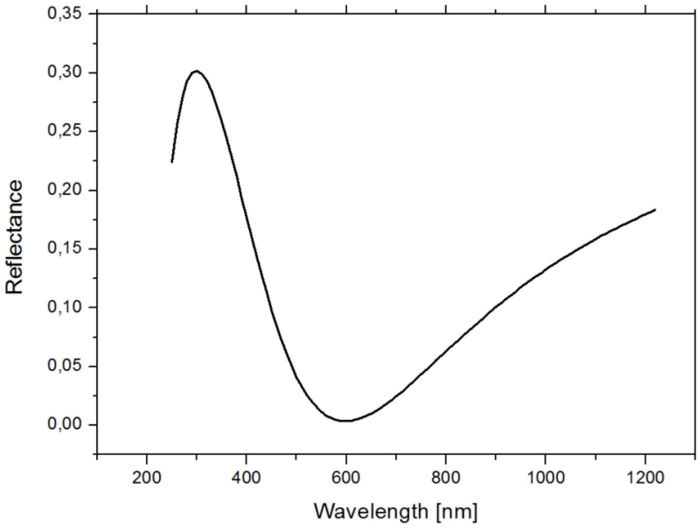

Figure 39: Expected reflectance after AR coating

It is seen from Figure 3 that at 600nm, the reflectance goes to zero while for a wide wavelength range, it is below 15%. These results clearly demonstrate the importance of the use of AR coating for an efficient solar cell device. In today's solar cells industry, a Si_3N_4 layer (n_s = 2.00) with a thickness of 80 nm is typically used as the anti-reflecting coating.

3.6.3. Experiment

In this work, thin film Si_3N_4 layer with refractive index 2.00 was deposited on Si wafers by Plasma Enhanced Chemical Vapor Deposition (PECVD) system at METU MEMS center (Figure 43). In a PECVD system, Si_3N_4 deposition is carried out by decomposition of the gases SiH_4 and NH_3 at relatively low temperatures (200-300 ^{o}C) in a plasma system shown in figure 40 below. The plasma is usually created by applying an RF signal with a frequency of 380 kHz.

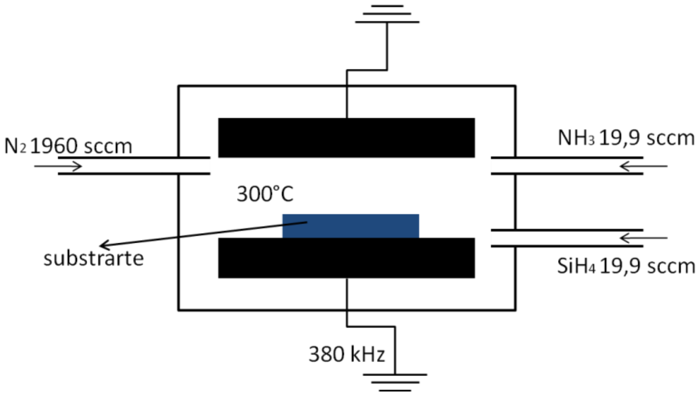

Figure 40: Schematic representation of PECVD

The chemical process during the coating is given as;

$$3SiH_4 + 4NH_3 \rightarrow Si_3N_4 + 24H_2 \tag{23}$$

From the consideration above, the desired thickness of the Si_3N_4 layer for the wavelength of 600 nm can be found as

$$t = \frac{\lambda}{4n_a} = \frac{600}{4 \times 2} = 75nm \tag{24}$$

We optimized the coating system to reach this thickness values. To demonstrate the thickness effect, several samples were coated with different thicknesses for reflectance measurements. After the coating, each film thickness was measured at 'Nanometrics-Nanospec-AFT Microarea Gauge' thickness gauge. Optical properties of the fabricated Si_3N_4 layers are presented in the next section.

3.7. Edge Isolation

3.7.1. Aim of Edge Isolation

The built in electric field across the junction separates the created electron hole pairs for current extraction form the solar cells. The electrons are collected from n type region and holes are collected from p type region in the solar cell operation.

During solid state diffusion, not only the front surface of the wafer but also edges and the back side of the cell are n-type doped. Although the Al back surface contact compensates the back side n layer, there still remain n-type regions on the edges and back side since whole back surface is not metalized [18] (Figure 41).

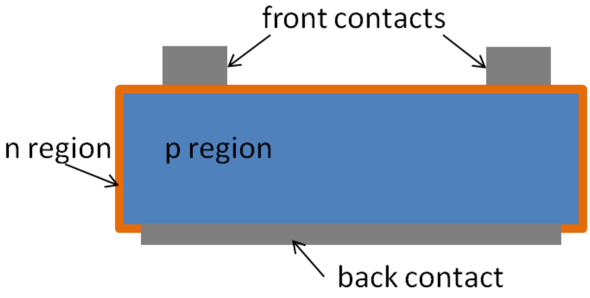

Figure 41: Solar cell before the edge isolation

This creates alternative paths for electrons and holes to recombine, which decreases the cell performance. Edge isolation solves shortcutting problem by electrically isolating the front and back sides of the cell should from each other. This is accomplished by either plasma etching of the edges or by laser scribing the front surface edges until p region as shown in figure 42.

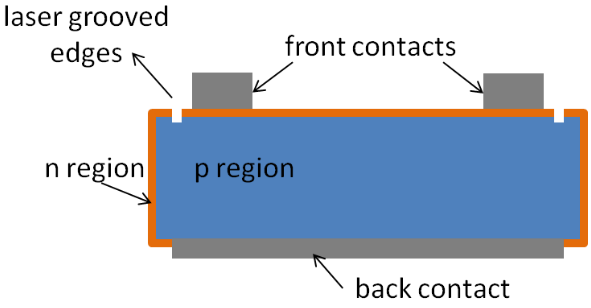

Figure 42: Cell with edge isolation completed by laser grooving from the front surface. Separated electron-hole pairs cannot recombine through back metal and n region contact.

3.7.2. Experiment

The edge isolation of the samples was made with 20W watt ND-YAG pulse laser at Nurol Technology factory. The wafers were placed at the holder with a height of 25.4mm in the laser cutter and the edges of the wafers were scribed at a speed of 400mm/s, with a pulse frequency of 10 kHz, one turn on each wafer at 90% power. Different focus lengths were tested to find the deepest groove on the surface.

3.7.3. Results

The change of groove depth with respect to focus length is given as in Figure 43.

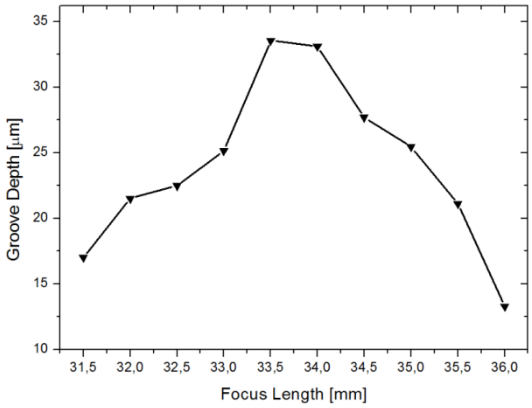

Figure 43: Groove depth vs. Focus length of the LASER used in edge isolation

The diameter of the laser grooved circle was 47mm (Figure 44). It is well known that 20µm depth is enough for edge isolation hence a focus length of 32mm was used on all wafers for edge isolation.

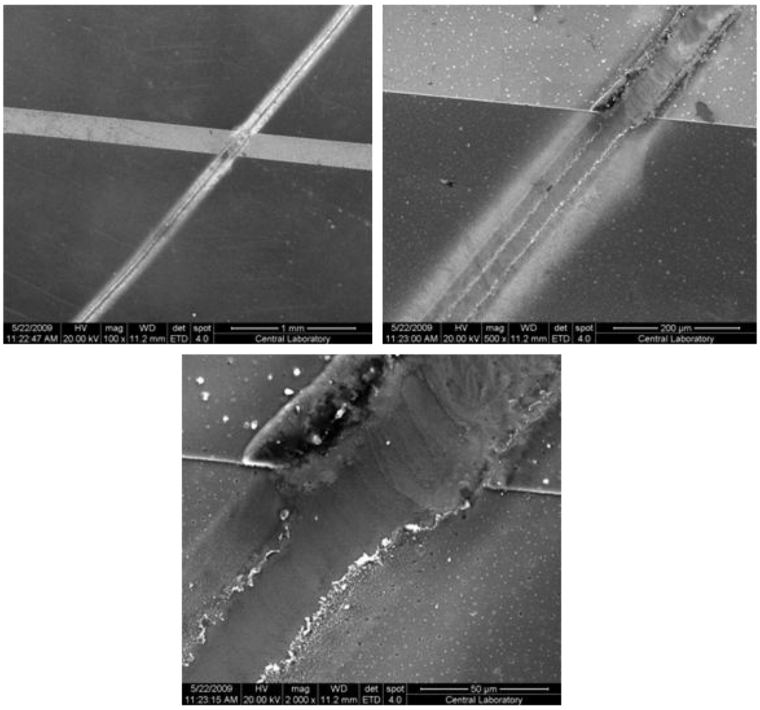

Figure 44: SEM images of LASER grooves for edge isolation

In standard process, edge isolation is the last step of cell production hence done on wafers with Si_3N_4 coating. The grooves on wafers with nitride coating showed better edge quality when compared to the directly grooved silicon (Figure 45).

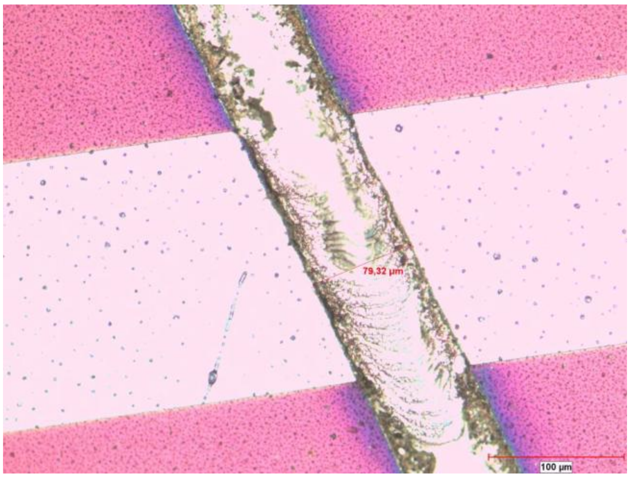

Figure 45: SEM image of LASER groove for edge isolation after AR coating

3.8. Summary and discussion

All steps related to single crystal silicon cell preparation were successfully completed in METU-MEMS clean room except the edge isolation which was carried out at Nurol Technology. The SEM images of textured samples showed that the desired surface patterns can be obtained by optimizing the process parameters. However, for final conclusions we need to evaluate the reflectance data presented in the next chapters. The different configurations of samples during diffusion showed that the position of wafers with respect to the gas flow inside the tube furnace affected the homogeneity of doping. Consequently, the alignment of wafers parallel to gas flow was chosen for better homogeneity. Moreover, the duration and the temperature parameters are studied for the best performance. The antireflective coating thickness was calculated for the wavelength of the maximum intensity of solar spectrum and Si_3N_4 films with this thickness were deposited on solar cells by PECVD. Different film thickness was tried for comparison. Edge isolation of the cells by laser grooving was optimized to obtain the best performance in the solar cells.

CHAPTER 4

CHARACTERIZATION

4.1. I-V Characteristics

4.1.1. Setup

The dark I-V characteristics of the solar cells were measured with a *Keithley Sourcemeter* controlled with PC via *Lab View.* The illuminated I-V characterization was performed with the system shown on Figure 46 with an *Oriel AM1.5G* solar simulator, a PC with software controlling the simulator and the *Keithley Sourcemeter* (Figure 46).

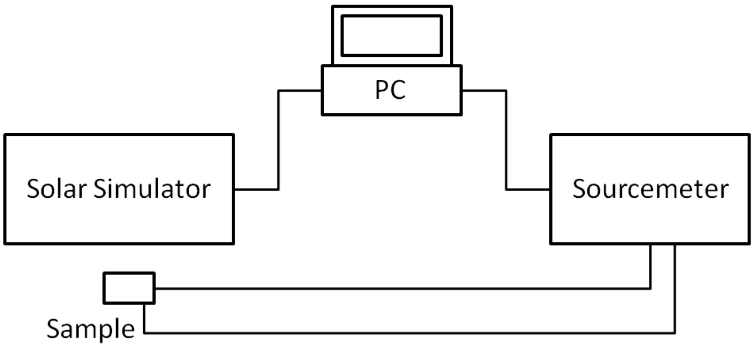

Figure 46: Experimental setup for I-V characterization

The solar simulator software analyses the measured I-V data and determines the efficiency, fill factor, max power point, short circuit current and open circuit voltage of the cells. The connections between the sample and the sourcemeter were formed by two probes from the front fingers and a cooper plate from the back side of the cell.

4.1.2. Results

For dark I-V measurements, we prepared special samples with front contact being in the form of circular dots. The back contacts are an Al film covering the whole back surface of the wafer. We have observed that the formation of p-n junction was successful, since the dark I-V curves exhibited typical diode behavior as shown in figure 47.

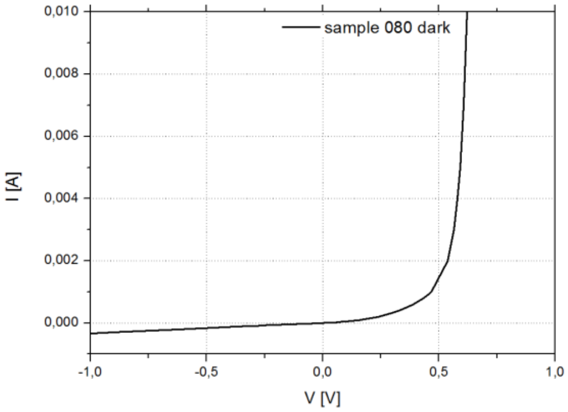

Figure 47 : Dark I-V curve for sample 080. The typical diode characteristics is seen

When the sample was illuminated, the I-V curve shifted along the vertical axis in the negative direction as shown in figure 48. This is showing the photovoltaic effect in the devices;

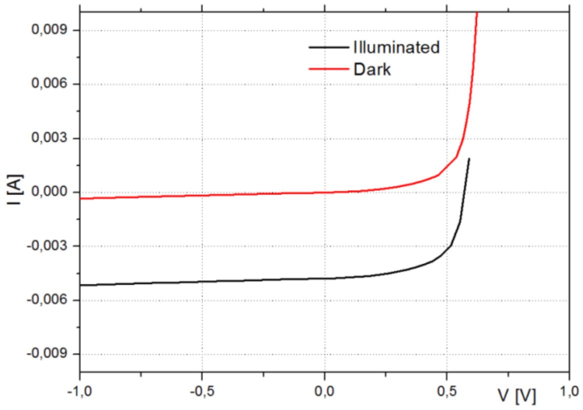

Figure 48: Illuminated(AM1.5G) and dark I-V results for sample 080 with an area of 0,18cm^2

We measured the I-V characteristics of the cells after each process step in order to see the effect of individual process steps. The I-V data before and after the edge isolation and AR coating are given in figure 49 and 50. We see that both process improved the cell performance significantly.

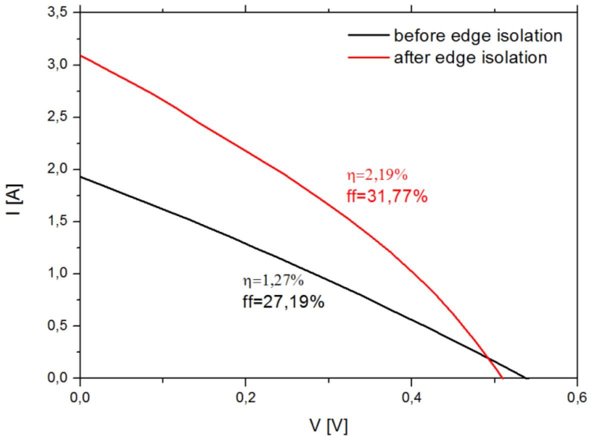

Figure 49: Effect of edge isolation on cell performance for sample 26 at AM1.5G. Sample area is 73cm^2 before edge isolation and 65cm^2 after edge isolation.

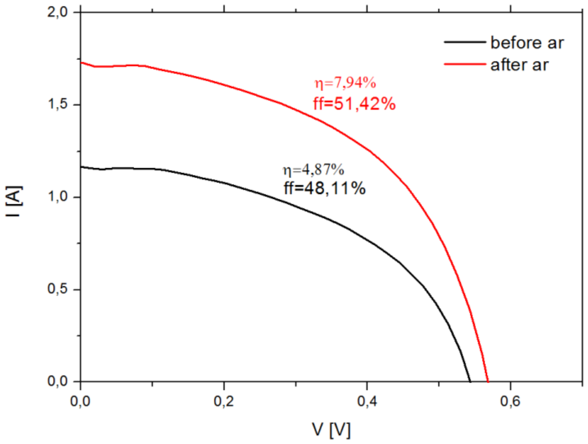

Figure 50: Effect of AR coating on cell performance for sample 083 with area of 65 cm^2 at AM1.5G.

We have also investigated the effect of annealing after the metallization on cell performance. Some selected samples were annealed at 450 °C for 30 min. The results showed that annealing was a very important step that completed the metallization for better contact performance (Figure 51).

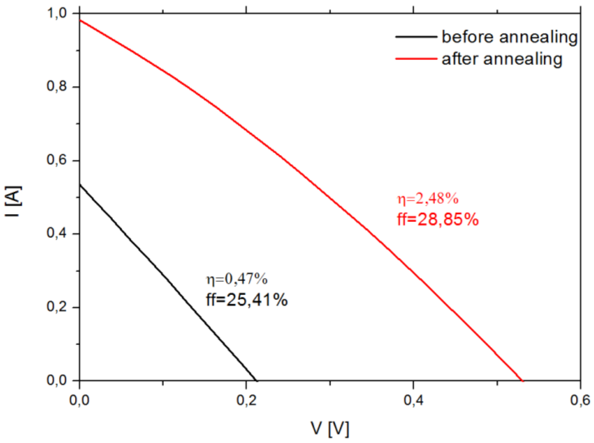

Figure 51: Effect of thermal annealing on performance of the sample 137 at AM1.5G with an area of 73cm^2.

The thickness of the metal contacts on the surface of the cells created by e-beam evaporation did not exceed 1-2µm, which causes a high series resistance. The effect of series resistance decreases as the cell dimension is decreased, since smaller amount of current would pass from the same contacts, meaning lower resistive losses. It was observed that, when the cell was broken into smaller pieces both fill factor and the efficiency of the cells improve significantly as shown in figure 52. The efficiency and fill factor values reach high values for the smallest cell pieces.

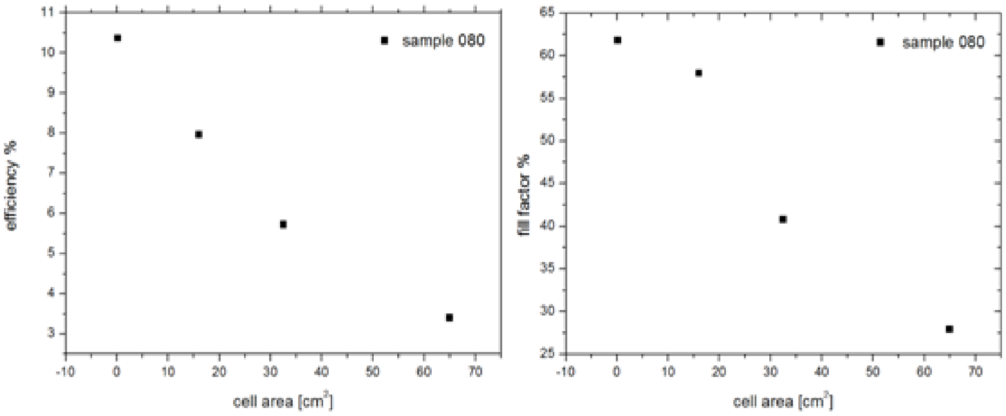

Figure 52: Effect of cell dimension on cell efficiency and fill factor at AM1.5G.

The effect of series resistance can also be inferred observed when the I-V curve in figure 53 is inspected. We see that, although the I-V curve shows a high fill factor, the efficiency is very low. This is due to a problem occurred during the metallization of the cell. Since the sample was textured, the etching of the thin metal layer on the front surface after photolithography was hard to control. Consequently the fingers and busbars were formed in a discontinuous way and the probes of the I-V tester only collected current from the point of contact from the cell. As the efficiency calculation is done using the whole cell area it is found to be very low compared to other samples. But at the same time the fill factor increased because the effective series resistance is reduced due to the point contact measurements.. The actual efficiency value would have been much higher if the area around the contact point could have been determined.

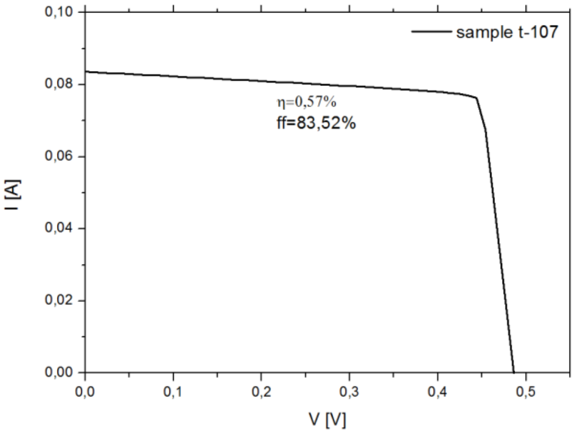

Figure 53: I-V curve for sample t-107 under AM1.5G. The metal contact is discontinuous and not properly formed. The efficiency value calculated by using the whole surface area does not reflect the actual value.

The I-V tests showed that metallization pattern also has effects on the cell performance. The two samples, sample 515 and 106 having exactly the same sheet resistivity and edge isolation parameters showed different performances under illumination as shown in Figure 54.

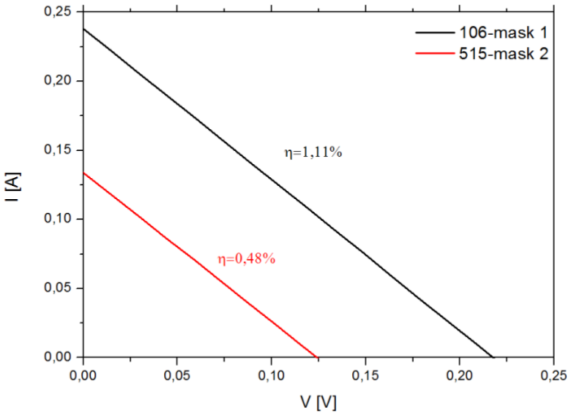

Figure 54: I-V curves for samples with different metallization patterns under AM1.5G with 65cm^2 area.

Result displayed in figure 54 showed that the mask 1 design yielded better performance therefore the metallization was carried on with this mask for later processes.

We studied the effect of sheet resistance on the open circuit voltages of the solar cells. Figure 55 displays the result of this study. We see that best voltage values were obtained with R_s values of 10-20 Ohm/□. The reason for this difference is likely to be related to the contact resistance between metal and semiconductor. At low R_s values the contact resistance is very low and we measure the voltage developed across the p-n junction only. For higher R_s values, the series resistance due to the resistance of the doped layer and the metal-semiconductor contact reduces the apparent open circuit voltage values.

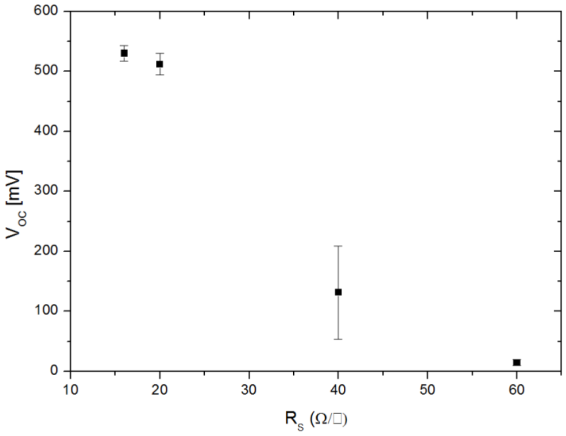

Figure 55: Open circuit voltage distribution with respect to sheet resistivity under AM1.5G spectrum for 65cm^2 cell area

4.2. Reflectance

4.2.1. Setup

The reflectance properties of the samples were measured with the system shown in Figure 56.

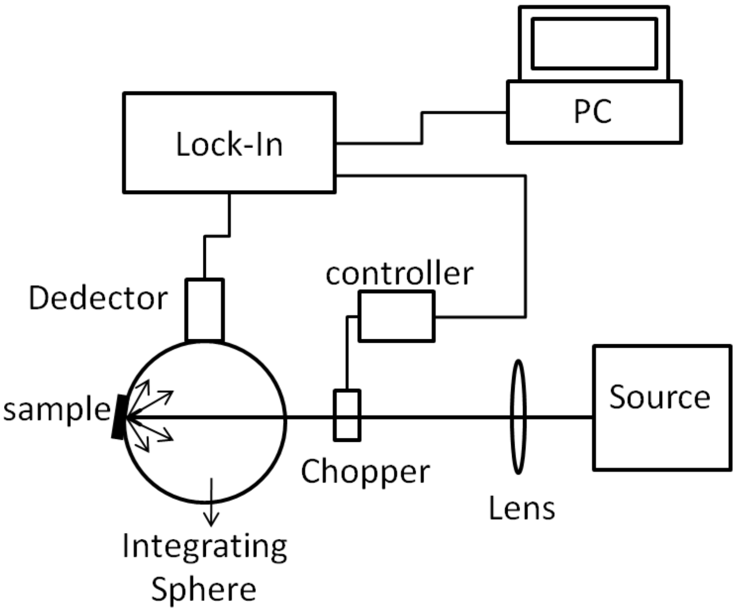

Figure 56: Reflectance measurement setup

The setup consisted of an *Oriel* integrating sphere, a *Stanford* lock-in amplifier, an *Oriel* chopper and controller, a calibrated *Oriel* silicon detector, an *Oriel* UV light source, focusing lens and a PC. The integrating sphere was used because the textured samples did not only have specular reflectance but also diffuse reflectance as illustrated in figure 57.

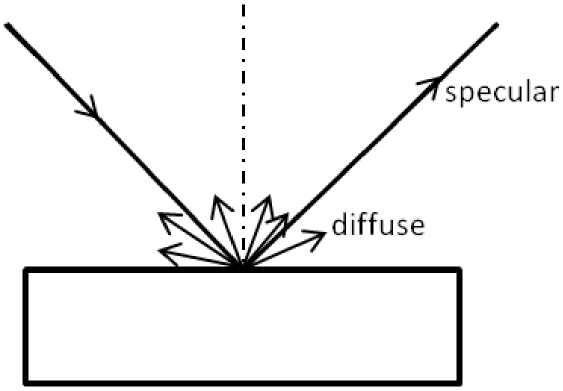

Figure 57: The incident beam undergoes both specular and diffuse reflectance.

In the integrating sphere, the sample is placed with a 4 degree rotation with respect to the incoming beam and the reflected beam creates a uniform illumination inside the sphere. For measurements, first a calibration disk was used as 100% reflectance reference and then the samples were measured. The ratio of the reflectance from the sample to the calibration disk gave the total net reflectance of the samples.

4.2.2. Results

The KOH texturing results showed that etching at %5 KOH solutions at 80°C for 45 minutes gives the closest results to the reflectance squared data of silicon${R_{Si}}^2$, which occurs due to double bouncing from the pyramidal textured surface as shown in figure 58. From this data, one can conclude that the best pyramid structure is obtained with this solution. This is indeed confirmed by the SEM pictures displayed in figure 22.

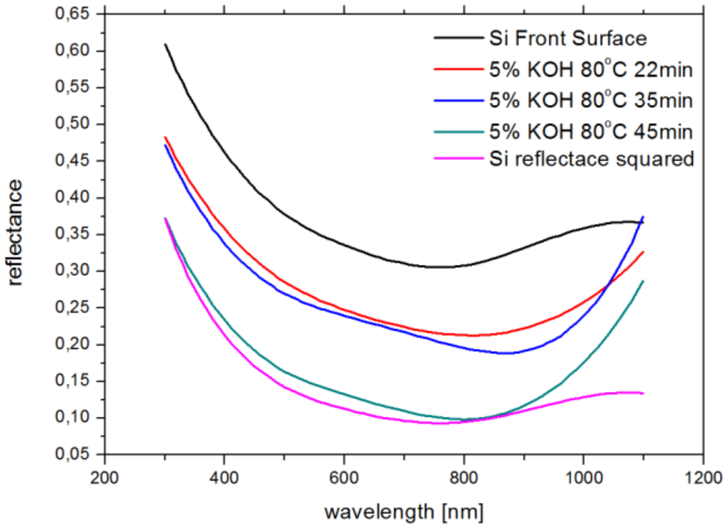

Figure 58: Reflectance data for different textured samples

We have reached this result after investigation of many samples processed with different solutions and durations. Figure 59 displays the results obtained from these samples. We see that %5 KOH solution at 80°C for 45 minutes gave the smallest reflectance results at 600nm

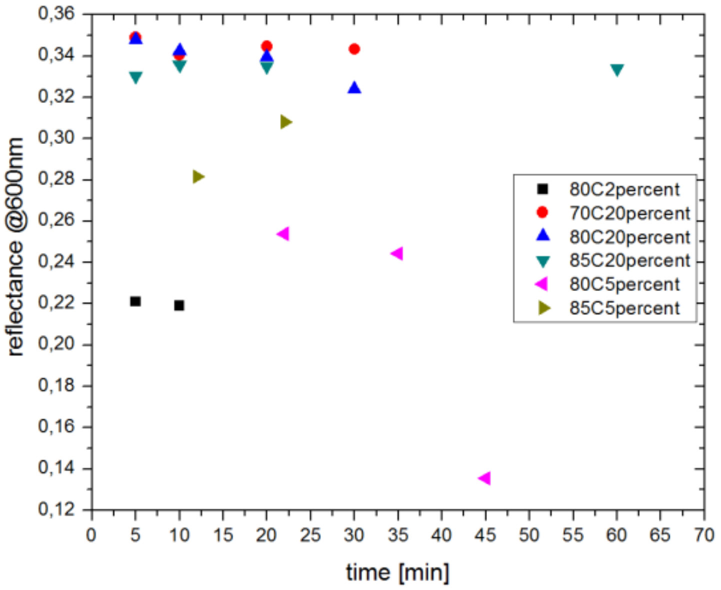

Figure 59: Reflectance @600nm for different samples textured with different parameters

Finally we present reflectance results for different AR layer thickness in figure 60. It is seen that the reflectance minimum shifts to higher wavelengths with increasing layer thickness as expected from the theoretical consideration given in the previous chapter.

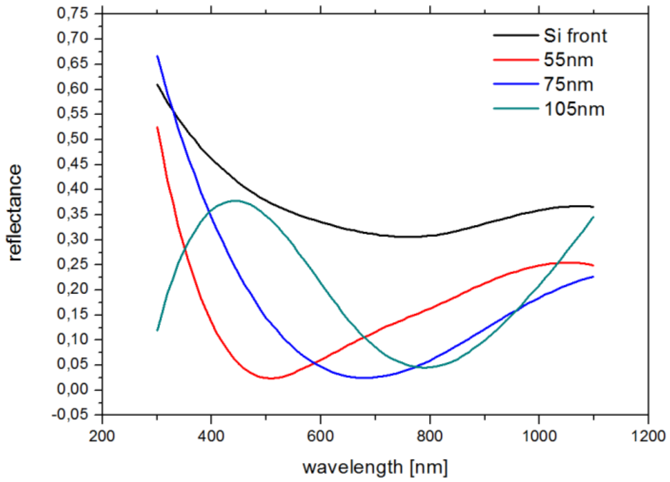

Figure 60: Reflectance of AR coated samples and Si

The reflectance results of three samples with 55nm, 75nm and 105nm thick Si_3N_4 thickness showed that reflectance spectrum has minimum values which can be calculated from the relation

$$t = \frac{\lambda}{4n_a} \tag{25}$$

The 75nm coating was expected to give minimum reflectance at 600 nm, however in the optical measurements it was seen that the minimum occurred at around 680nm. This shift may be due to an error in the thickness measurement. If this is the case the actual thickness of the coating is found as

$$t = \frac{\lambda}{4n_a} = \frac{680}{4x2} = 85nm \tag{26}$$

4.3. Quantum Efficiency

4.3.1. Setup

Quantum efficiency experiments were conducted with the setup shown in Figure 61.

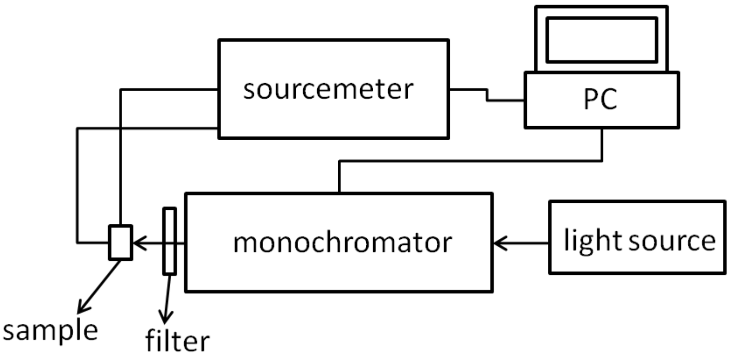

Figure 61: Quantum Efficiency measurement setup

Setup consisted of a halogen light source, an *Oriel* monochromator controlled with a PC, an *Oriel* high pass filter to avoid second harmonics, a *Keithley* source meter and a PC. The samples were prepared in such a way that they had surface areas smaller than the area of the light beam incident from the monochromator. Since the power density output of the monochromator was measured before, the power incident on the surface of the cell could be calculated simply by multiplying the area of the cell with the power density at that wavelength. Then after simple calculations, the number of photons incident on the cell surface at each wavelength is found. The measurements of source meter yielded the current output at each wavelength which gave the number of electrons collected. Finally, the quantum efficiency is calculated by using the relation

$$QE = \text{number of carriers collected / the number of photons incident.} \qquad (27)$$

4.3.2. Results

The external quantum efficiencies of three samples are shown in Figure 62.

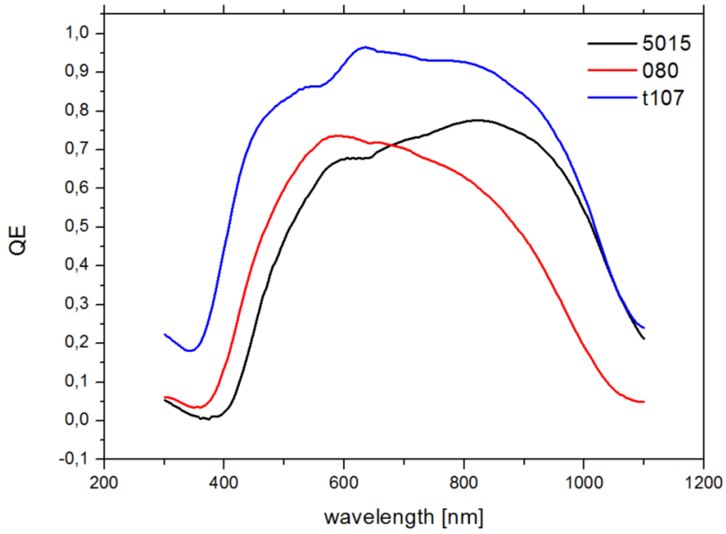

Figure 62: QE curves for four different samples.

Table 4 shows the properties of three samples whose QE curves are given in Figure 62.

Table 4: The properties of samples with QE shown in Figure 62

	Rs [Ω/□]	Surface Texturing	AR Coating
5015	10,2	Not applied	Not applied
080	20	Not applied	85 nm Si_3N_4
T107	65	Applied	85 nm Si_3N_4

It is seen from the QE graph that sample t107, with texturing and AR coating, has the highest conversion efficiency among other samples.

When the internal quantum efficiencies of samples 080 and 5015 is compared (Figure 63), it is seen that sample 5015 has better conversion efficiency than 080. However antireflective coating applied on sample 080 brings the overall quantum efficiency of 080 close to 5015 which shows the effect of AR coating on cell performance.

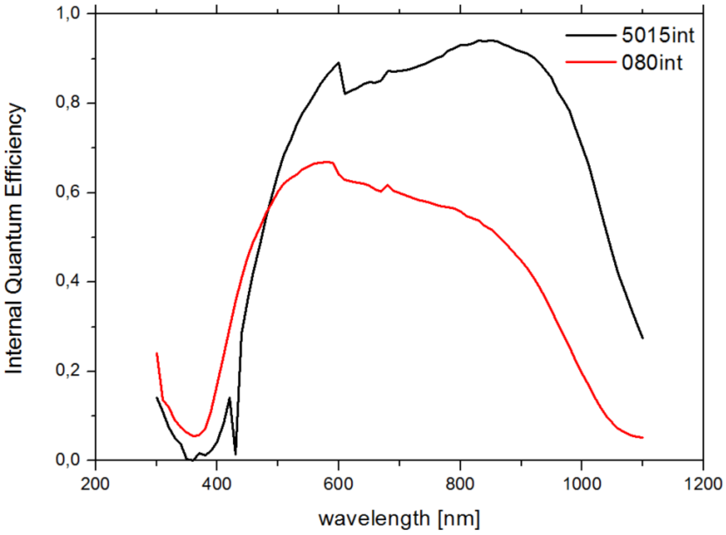

Figure 63: Internal Quantum Efficiencies of two samples

Sample 080 has better response for smaller wavelengths due to Si_3N_4 coating which decreases front surface recombination by passivation. However 5015 has better performance totally due to better contact formation because of high doping levels.

4.4. Summary and discussion

The results of characterization data showed that;

- The mask 1 design with narrower finger widths yielded better performance due to less shadowing losses
- The edge isolation of the cells had a strong effect on cell performance by avoiding shunts
- AR coating also increased the cell efficiency by decreasing reflectance and passivation of the front surface
- The annealing step after metallization helped a better contact formation

- The metallization by evaporation which did not exceed 1-2µm was not enough to carry current generated by cells which is more than 1,5A hence most of the power generated was dissipated by metal contacts
- The Al front side contacts on surfaces with 10-20 Ώ/□ sheet resistances gave the best results
- The calculated AR coating thickness gave the expected minimum at expected wavelength which was close to 0%
- The texturing was succeeded with the observation of double bounce effect from reflectance results
- The sample with texturing, AR coating had the best quantum efficiency both due to high light trapping ability and low wafer thickness coming from long etching duration.

CHAPTER 5

SELF ASSEMBLY FORMATION OF GOLD NANOPARTCLES TO ENHANCE LIGHT TRAPPING USING LOCALIZED SURFACE PLASMON EFFECT

5.1. Introduction

The importance of light trapping for solar cells and the method of enhancing light trapping for single crystal silicon solar cells were discussed in section 3.1. where surface texturing was applied to form micro pyramid structures. Another method, which is attracting a lot of attention in recent years, is the use of localized surface plasmons in metal nanoparticles. The metal nanoparticles located on the front surface of the solar cells scatter incoming light into the solar cell reducing reflection and increasing light trapping [18]. Although the light trapping abilities of the method seem to be not superior when compared to anisotropic etching in single crystalline thick silicon solar cells, its usage will be a solution for light trapping problems in crystalline solar cells fabricated on thin wafers or in thin film solar cells.

Metal nanoparticles can be formed on the surface of the solar cells in different ways. One way is the use of electron beam lithography to create arrays of metal nanoparticles on the cell surface, which provides well defined particle dimension and geometry. But this method is not suitable for the mass production. The other method is to apply self assembly formation in which the metal particles are formed on the surface by annealing a thin layer of the metal film predeposited on the wafer surface. Although the particle dimension and geometry is not well controlled, this method is more suitable for large area deposition and mass production.

5.2. Theoretical Considerations

At plasmon resonance frequencies, the metal nanoparticles scatter the light strongly due to oscillations of free electrons in the metal. The scattering and absorption cross sections for particles with dimensions below the wavelength are given with point dipole approximation as [19];

$$C_{scatt} = \frac{1}{6\pi}\left(\frac{2\pi}{\lambda}\right)^4 |\alpha|^2, \quad C_{abs} = \frac{2\pi}{\lambda} Im[\alpha] \tag{27}$$

Where the polarizabilty is defined as;

$$\alpha = 3V\left[\frac{\varepsilon_p/\varepsilon_m - 1}{\varepsilon_p/\varepsilon_m + 2}\right] \tag{28}$$

In equation 28, e_p is the dielectric function of the particle e_m is the dielectric function of the medium and V is the volume of the particle. When $e_p = -2e_m$ the scattering and the absorption cross-sections become very large and this is known as the surface plasmon resonance. The scattering, which is desired for solar cell applications, is more efficient than absorption for larger particle sizes due to $|\alpha|^2$ factor which depends on volume of the particle [19].

In this part of the work, we investigated the fabrication of metal nanoparticles by self assembly method, and their optical properties by reflection experiments.

5.3. Experiment

For experiments, 100 oriented, 4” single crystalline Si wafers with 5-10Ω -cm B doping were used as substrates. The wafers were coated with 25nm of gold film using thermal evaporation and after coating the samples were annealed at different temperatures and durations in tube furnace under N_2 flow of 110 SCCM. After the annealing the reflectance properties of the samples were studied with the setup used in section 4.2. (Figure 56) Particle size and distribution were studied by analyzing the SEM pictures that were taken for each sample.

5.4. Results

Figure 64 shows the SEM image of the sample annealed at 300 ^{o}C for 60 min. We see from this SEM picture that the formation of metal nanoparticles was successfully achieved after annealing

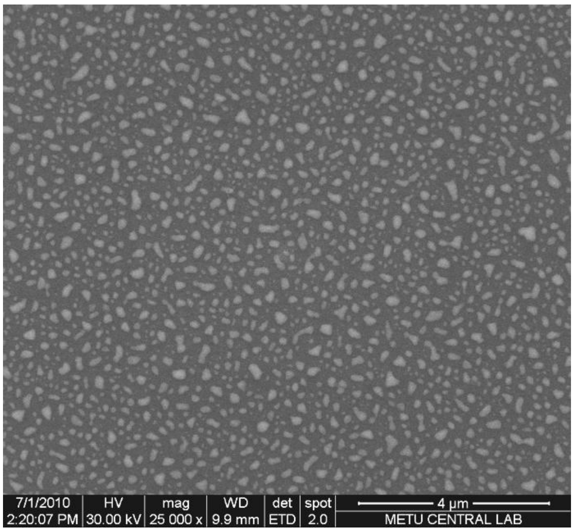

Figure 64: SEM image of sample annealed at 350°C for 60 minutes

It is also seen from the same picture that there is a random distribution of gold nanoparticles on the surface of the wafer. In order to analyze the size distribution, , an image processing script was written using *MATLAB* the source code of this program is given in Appendix 1. , The percentage coverage and dimensional information were obtained using this program. The first observation is that when temperature is constant the annealing duration did not have a drastic effect on particle dimension (Figure 65).

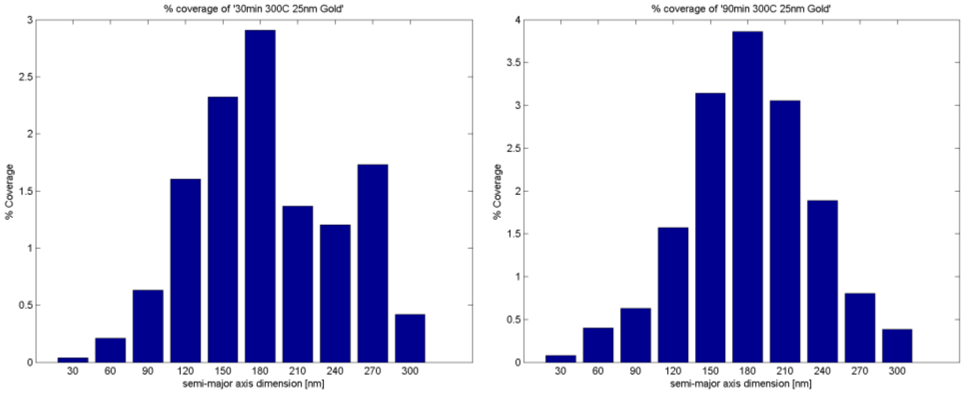

Figure 65: % Surface coverage of particles with different dimensions at 300°C for 30 and 90 minutes

On the other hand, the mean particles increase with annealing temperature as shown in figure 66.

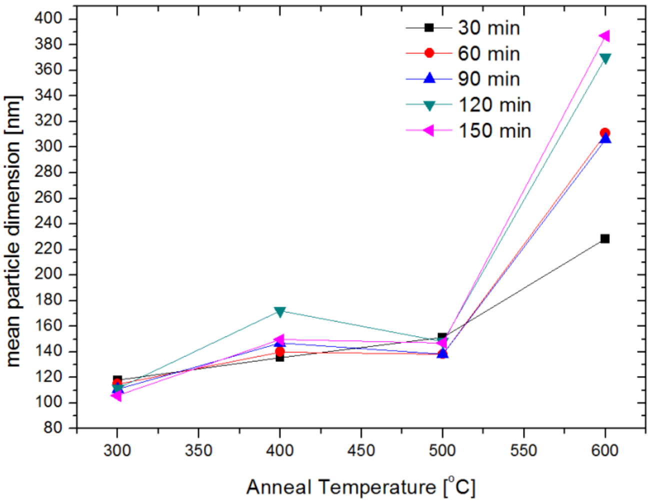

Figure 66: The mean particle sizes vs. different annealing temperatures.

The surface coverage percentages shown in table 5 did not show any systematic variation although it generally lies between 10-20%. These values are quite acceptable because the scattering cross section could be 10 times larger than the particle size. This means that 10% coverage would be sufficient to scatter from the whole surface area [19].

Table 5: The surface coverage percentage values for samples at different temperatures and annealing durations

	30 minutes	90 minutes	150 minutes
350°C	17,68	18,14	19,12
500°C	15,23	15,96	11,5
600°C	11,84	9,86	10,6

In order to see the scattering properties, the reflectance spectra of the nanoparticles were obtained. It is seen from figure 67 that the anneal duration did not have any particular effect on the reflectance spectrum. This corresponds to the fact that 30 minutes is long enough for self assembly formation and once the particles are formed, they do not interact with each other to form bigger or smaller sized particles. This is in agreement with the results obtained from the SEM images displayed in figure 66.

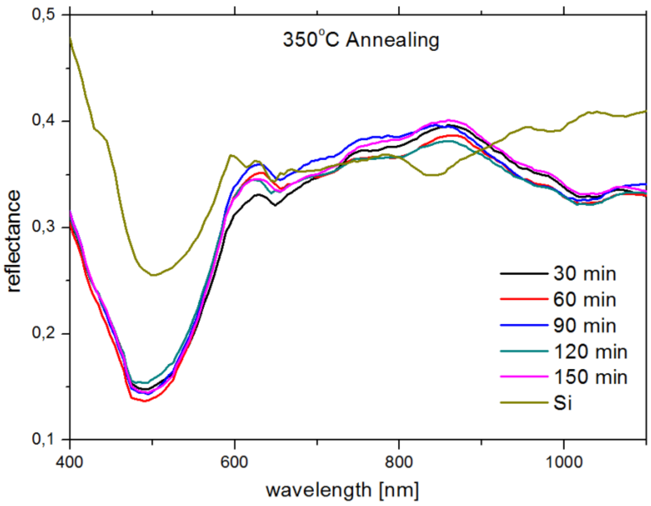

Figure 67: Reflectance spectrum for samples annealed at 350°C for different durations and for Si.

The effect of anneal temperature on reflectance spectra is shown in figure 68. The normalized reflectance spectra of the samples with gold nanoparticles are compared with the reflectance spectra of the bare Si wafer and with the as deposited wafer [20]. The reflectance value of as deposited gold is very high when compared to annealed samples therefore the reflectance values for this sample type are multiplied with 0.5 for a better comparison.

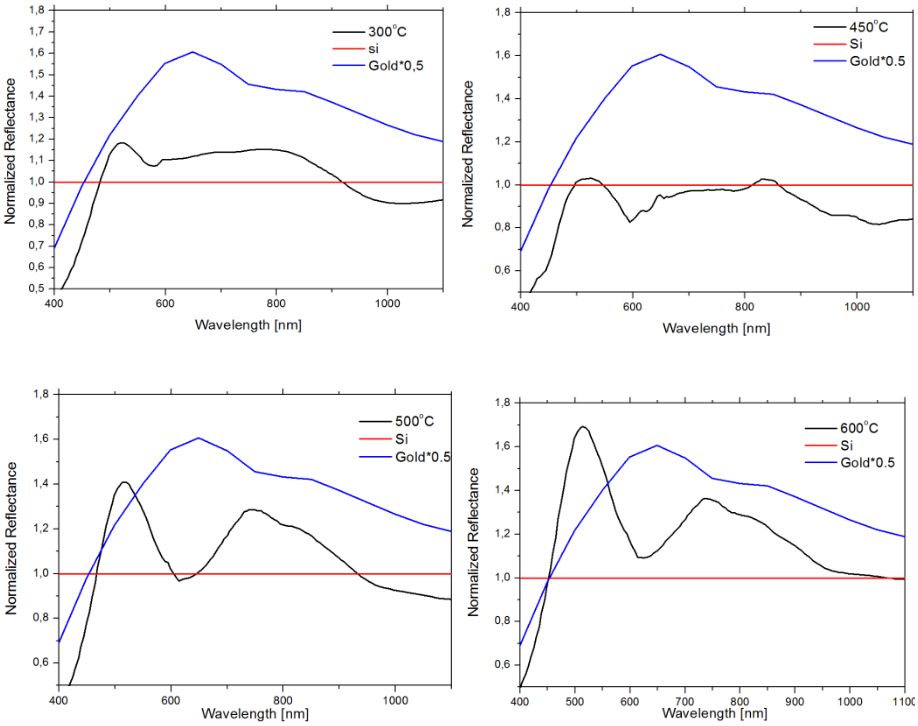

Figure 68: Normalized reflectance spectra for samples with and without gold film and the sample annealed at four different temperatures for 1 hour.

It is seen form figure 68 that at 300°C, the annealed sample had a spectrum close to as grown gold; however as the temperature is increased two scattering peaks become distinctive. These two peaks correspond to the resonance plasmonic scatterings from the large area gold surface and from the localized surface scattering respectively. When the surface coverage of those samples are investigated (Figure 69), it is seen that, as the temperature increases, the standard deviation on particle size is also reduced therefore samples annealed at high temperatures have more uniform size distribution. The first peak occurring at 515-520 nm is attributed to the plasma frequency of continuous gold films. The second peak at longer wavelength is due to the plasmon resonance of the nanoparticles. This scattering peak has been observed from nanoparticles having similar dimensions [Urcan's thesis]

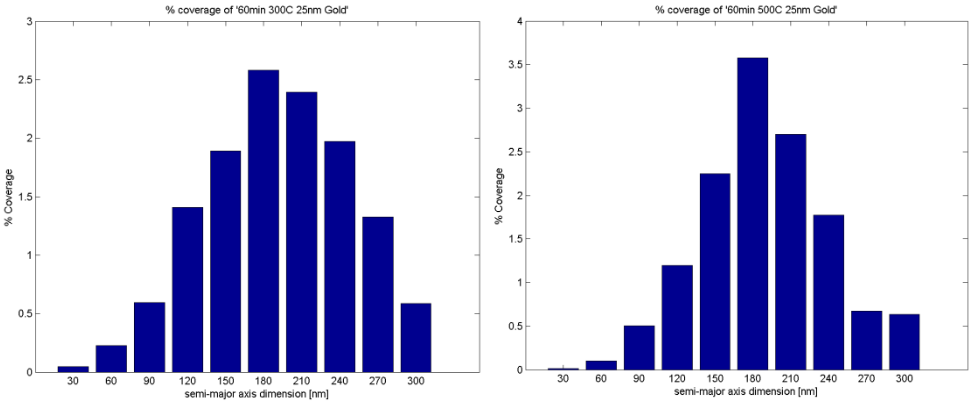

Figure 69: The % coverage values for two samples annealed at 300°C and 500°C for 1 hour. As the temperature increases, the deviation on particle dimension is decreased.

5.5. Summary and Discussion

The effect of gold nanoparticles on light trapping by surface plasmon resonance is an ongoing subject to enhance solar cell efficiency. The nanoparticles radiating at surface plasmon resonance behave like small antennas which absorb light and re-emit in all directions back. If the re-emission is completed at more than critical angles, the light trapping ability is expected to increase.

During this study, self assembly formation of gold nanoparticles on large area by temperature annealing has been studied. It has been observed that 30 minutes of annealing is sufficient for nanoparticle formation and increase of anneal duration did not have any further effect on mean particle size or dimensional spread of particles. It has been observed that as the temperature is increased, the reflectance peaks become more pronounced as a result of better particle definition. The observed scattering peaks, the first one at 515nm and the second one at 740nm, are attributed to plasma frequency of gold and the surface plasmon resonance of gold nanoparticles respectively.

The reflectance spectra only show the re-emitted light from the surface. They do not give any data about the transmitted light. No observation about the transmission can be done with Si wafers in visible region. However, of the scattering peaks seen in the reflectance spectra is an evidence of surface plasmon resonance and scattering from the nanoparticles. A more detailed analysis should include thin wafers and/or thin film structure. Also the technique should be tested with a solar cell structure..

CHAPTER 6

CONCLUSION

Photovoltaic conversion has become one of the most promising alternatives for electricity production due to its clean nature, low maintenance costs and long term stability. Crystalline wafer silicon technology has been one of the most cost efficient and commonly used technologies in photovoltaics. This is due to the fact that silicon has been used for micro electronics for more than 30 years and is a very well known material. Today the standard technology reaches 22% with back contact back junction design at cell base and 19% at module base.

The aim of this thesis is to be able understand the basic solar cell structure with all production and characterization steps. The cells were fabricated at METU-MEMS facility clean room and characterized at METU Physics Department and METU Central Lab. For production 4" single crystal CZ, boron doped p type, electronic grade wafers with 525µm thickness at (100) orientation are used. The light trapping abilities of the solar cells are enhanced by surface texturing and random pyramid formation at KOH solution. The SEM images showed that pyramid formation is succeeded. The cleaning of the wafers before solid state diffusion is carried in 4 steps including HF, RCA1 and RCA2 cleaning steps. The formation of p-n junction is completed at open end diffusion furnaces with $POCl_3$ as phosphorus source at temperatures between 800-900°C. Effects of different diffusion procedures at cell performance are tested. The metallization is competed at several steps different than screen printing and firing which are standard processes. The front surfaces of the wafers are coated with Al and then the front grid pattern is formed by photolithography. Than the back surfaces of the cells are also coated with Al for back contact formation. An annealing step at low temperatures followed the metallization for better contact formation. Different metal patterns are also used to see the effect on cell performance. The wafers are then coated with Si_3N_4 as an anti-reflective coating and front surface passivation. The shorts between front n side and back p side are avoided by laser edge isolation.

The I-V characteristics of the cells are tested with Oriel Solar Simulator under AM1.5G condition and the effects of edge isolation, annealing, metal pattern, anti-reflective coating and sheet resistivity are investigated. The reflectance characteristics of the samples are measured at an Oriel integrating sphere and texturing and anti-reflective coating performances are examined. SIMMS profiles of the cells to see junction formation are taken and evidence for junction formation is seen. Quantum efficiencies of the cells are measured with an Oriel monochromator and Keithley source.

The texturing, anti-reflective coating, metallization, edge isolation and diffusion steps have all been covered and optimum values for these processes has been found. The best efficiency reached during the study is 10% under AM1.5G condition for $0.18cm^2$. The reason for this low efficiency compared to industrial cells is that the standard process included different metallization techniques and thinner wafers which decrease series resistance and recombination respectively.

A promising alternative of surface texturing for light trapping at solar cells is also investigated. Samples are coated with thin layers of gold and annealed at different temperatures and different durations for self assembly formation of gold nano-particles. Formation of gold nano-particles is observed by SEM pictures and statistical data is collected from these pictures about gold nanoparticles. Then the effect of the nanoparticles on reflectance spectrum is analyzed. The effect of surface plasmon peaks is observed from resonance peaks however further study is necessary to observe sharper peaks and position control of the peaks.

For further studies screen printing and firing processes for metallization has to be observed in order to reach standard cell results. In addition the wafer thickness must be decreased to decrease recombination losses. Also different metallization patterns such as metallization wrap through and emitter wrap through can be studied. More statistical analysis should be done on gold nanoparticle formation and their effect on cell performance has to be also investigated.

BIBLIOGRAPHY

[1]- D. Mills. “Advances in solar thermal electricity technology” Science Direct Solar Energy 76 (2004): 19-31.

[2]- University of Delaware. “University Of Delaware-Led Team Sets Solar Cell Record” Science Daily 30 July 2007. Web. 8 February 2010

[3]- Luque Antonio, Hegedus Steven. “Handbook of Photovoltaic Science and Engineering.” England: Wiley, 2003

[4]- *“NREL Best Research Cell Efficiencies” Web. 22.08.2010 15.23 http://nachhaltiger.net/index.php/2010/03/news/best-research-cell-efficiencies-national-renewable-energy-laboratory-usa1jpg-png-image-1332x811-pixels/*

[5]- I Kaizuka, G Watt, P Hüsser, P Cowley & R Bründliner. “Trends in photovoltaic applications – latest results from the IEA PVPS programme surveys”. 23rd European Photovoltaic Solar Energy Conference, Valencia 2008, 3641-3644

[6]- EPIA “Global Market Outlook for Photovoltaics Until 2014, May 2010 Update”

[7]- William P. Hirschman, “Cell Technology Shares” Photon International PHOTON MAGAZINE. 3-2009

[8]- *“Single Crystal Silicon Solar Cell”* Web. http://sovoxglobal.com/cell_classification.html 22.08.2010 15:30

[9]- Ineke Malsch. “Thin films seek a solar future”. The Industrial Physicist Magazine, Vol.9 p16, 2003

[10]- University of California - Santa Barbara. "Higher Efficiency Organic Solar Cell Created." Science Daily 15 July 2007. Web. 2 March 2010

[11]- “AM1.5 Spectrum” Web. http://rredc.nrel.gov/solar/spectra/am1.5, 05.07.2010 21:07

[12]- “*Reference Solar Spectral Irradiance: ASTM G-173” Web.* http://rredc.nrel.gov/solar/spectra/am1.5/ASTMG173/ASTMG173.html, 23.05.2010, 14.29

[13]- *“Appendix.3. Optical Properties of Silicon”*

Web. http://pvcdrom.pveducation.org/APPEND/OPTICAL.HTM, 23.05.2010, 15.18

[14]- Jenny Nelson, *“The Physics of Solar Cells”* Mono Crystalline Solar Cells P.189, Imperial College, Press 2003

[15]- Micro Chemicals, “Wet Etching of Silicon.” Web. www.microchemicals.eu/technical_information, 15-12-2009

[16]- *“Appendix.3. Optical Properties of Silicon”*

Web. http://pvcdrom.pveducation.org/APPEND/OPTICAL.HTM, 20.06.2010, 16:30

[17]- *“Appendix.3. Optical Properties of Silicon”*

Web. http://pvcdrom.pveducation.org/APPEND/OPTICAL.HTM, 23.05.2010, 15, 18

[18]- Ing. Ludger Müllers, Ing. Richard Hendel, Dr.-Ing. Roland Mayerhofer , “Analysis Of Different Laser Concepts For Edge Isolation Of Crystalline Solar Cells”.
ROFIN / Baasel Lasertech Petersbrunner Str. 1b, 82319 Starnberg, Germany

[19]- K.R. Catchpole, A. Polman, “*Plasmonic solar cells*”. Optical Society of America 2008

[20]- Otto Loebich, “*Optical Properties of Gold a Review of Their Technical Utilisation”.*

Gold Bull, 1972

APPENDIX A

MATLAB CODE FOR IMAGE PROCESSING

```
%%%%%%%%%%%%%%%%%%%%%%%%%%%%%%%%%%%%%%%%%%%%%%%%%%%%%%%%
% A MATLAB program for processing and analysis of nanoparticle images taken at SEM%
%%%%%%%%%%%%%%%%%%%%%%%%%%%%%%%%%%%%%%%%%%%%%%%%%%%%%%%%

Clear
clc

file= input('please enter the name of the picture ','s');    %input the target image name

flnm1=input('please enter the name of destination file 1 ','s');    %output destination 1
flnm2=input('please enter the name of destination file 2 ','s');    %output destination 1
flnm3=input('please enter the name of destination file 3 ','s');    %output destination 1
flnm4=input('please enter the name of destination file 4 ','s');    %output destination 1
name= input('please enter the sample name','s');                    %sample name

i = imread(file);             %read image to i
figure,imshow(i);             %show resulting image

i2 = imcrop(i,[0,0,1024,880]);        %crop the legend
figure,imshow(i2);                    %show resulting image

i3 = rgb2gray(i2);       %convert to grayscale
```

```
figure,imshow(i3);     %show resulting image

i4 = imopen(i3,strel('disk',20));             %select background
figure,imshow(i4);                            %show resulting image


i5 = imsubtract(i3,i4);  % subtract background from original to have uniform background contrast
%figure,imshow(i5);    %show resulting image

i6 = imadjust(i5);          %adjust contrast
figure,imshow(i6);       %show resulting image

level = graythresh(i6);  %convert to binary
i7 = im2bw(i6,level);     %convert to black and white
figure,imshow(i7);       %show resulting image

i8 = imopen(i7,strel('disk',2));      %select sizes with pixel>2
figure,imshow(i8);                    %show resulting image

[labeled,numObjects] = bwlabel(i8,4);
clc

number=numObjects;               % number of objects in image
fprintf('# of particles : %d\n',number);     %output  # of particles

graindata = regionprops(labeled,'basic');

maxArea = max([graindata.Area]);         %find the biggest area particles
meanArea = mean([graindata.Area]);     %find the mean area of particles
```

```
mjr=regionprops(labeled,'MajorAxisLength');          %major axis of nanoparticles
mnr=regionprops(labeled,'MinorAxisLength');          %minor axis of nanoparticles
circularity = [mnr.MinorAxisLength]./[mjr.MajorAxisLength];     % define circularity


figure, hist(circularity,10);                        % draw circularity vs frequency and save
xlabel('circularity');                               % to harddisk
ylabel('frequency');
ttl1=title(['circularity of ', name]);
set(ttl1, 'Interpreter', 'none') ;
saveas(gcf,flnm1);
close;

orien=regionprops(labeled,'Orientation');            % orientation

figure, hist([orien.Orientation],10);                % draw orientation vs frequency and save
xlabel('angle of major axis with horizontal');       % to harddisk
ylabel('frequency');
ttl2=title(['Orientation of ', name]);
set(ttl2, 'Interpreter', 'none') ;
saveas(gcf,flnm2);
close;


lngth = [mjr.MajorAxisLength];
lngth = 5.83*lngth;

figure, hist(lngth,10);                              % draw dimension vs frequency and save
xlabel('semi-major axis dimension [nm]');            % to harddisk
```

```
ylabel('frequency');
ttl1=title(['dimension distribution of ', name]);
set(ttl1, 'Interpreter', 'none') ;
saveas(gcf,flnm3);
close;

totalcoverage=sum([graindata.Area])/901120

meanlength=mean(lngth)                   %output mean dimension
sd1=lngth-meanlength;
sd2=sd1.*sd1;
sd3=mean(sd2);
standartdeviation=sqrt(sd3)              %output standart deviation

coverage=[graindata.Area]/901120;        %define coverage

bin1=0;                                  %define bins with zero initial
bin2=0;
bin3=0;
bin4=0;
bin5=0;
bin6=0;
bin7=0;
bin8=0;
bin9=0;
bin10=0;

[m,n]=size(lngth);                %define coverage matrix

for i=1:1:n                       %fill the bins
```

```
if lngth(i)<30&&lngth(i)>0
bin1=bin1+coverage(i);
else
if lngth(i)<60&&lngth(i)>30
bin2=bin2+coverage(i);
else
if lngth(i)<90&&lngth(i)>60
bin3=bin3+coverage(i);
else
if lngth(i)<120&&lngth(i)>90
bin4=bin4+coverage(i);
else
if lngth(i)<150&&lngth(i)>120
bin5=bin5+coverage(i);
else
if lngth(i)<180&&lngth(i)>150
bin6=bin6+coverage(i);
else
if lngth(i)<210&&lngth(i)>180
bin7=bin7+coverage(i);
else
if lngth(i)<240&&lngth(i)>210
bin8=bin8+coverage(i);
else
if lngth(i)<270&&lngth(i)>240
bin9=bin9+coverage(i);
else
if lngth(i)<300&&lngth(i)>270
bin10=bin10+coverage(i);
end
```

```
end
end
end
end
end
end
end
end
end
end
q=[bin1;bin2;bin3;bin4;bin5;bin6;bin7;bin8;bin9;bin10];
q=q*100;
r=[30;60;90;120;150;180;210;240;270;300];


figure, bar(r,q);                                          %draw coverage vs % and save to disk
xlabel('semi-major axis dimension [nm]');
ylabel('% Coverage');
ttl1=title(['% coverage of ', name]);
set(ttl1, 'Interpreter', 'none') ;
saveas(gcf,flnm4);
close;
```